Title: Niche exclusion of a lung pathogen in mice with designed probiotic communities

Authors: Kelsey E Hern[1], Ashlee M Phillips[2], Catherine M Mageeney[3], Kelly P Williams[4], Anupama Sinha[3], Hans K Carlson[5], Kunal Poorey[4], Nicole M Collette[2*], Steven S Branda[3**], Adam P Arkin[5,6,7***]

Affiliations:

1. Department of Plant and Microbial Biology, University of California Berkeley, Berkeley, CA, United States
2. Division of Biosciences and Biotechnology, Lawrence Livermore National Laboratory, Livermore, CA, United States
3. Department of Biotechnology and Bioengineering, Sandia National Laboratories, Livermore, CA, United States
4. Department of Systems Biology, Sandia National Laboratories, Livermore, CA, United States
5. Division of Environmental Genomics and Systems Biology, Lawrence Berkeley National Laboratory, Berkeley, CA, United States
6. Department of Biological Engineering, University of California Berkeley, Berkeley, CA, United States
7. aparkin@lbl.gov

Corresponding author email address:
*** collette2@llnl.gov**
**** sbranda@sandia.gov**
***** aparkin@lbl.gov**

Summary

For years, the airway microbiota have been theorized to be gatekeepers of respiratory health, as pathogens entering the airway make contact with resident microbes prior to or coincident with their interaction with host cells. Thus, modification of the native airway community may serve as a means of altering the local environment in favor of health. In this work, we hypothesize that synthetic bacterial communities introduced into the airway can serve as prophylactic countermeasures against infection by *Burkholderia thailandensis* in mice. We demonstrate that understanding of antagonistic interactions between a pathogen and airway microbiota *in vitro* can guide identification of probiotics with protective capabilities *in vivo*. Specifically, we show that niche overlap between the probiotic and pathogen is indicative of probiotic performance *in vivo*. This work serves as a foundation for the rational design of probiotic communities for protection against and treatment of respiratory infections.

Keywords

microbiome engineering, probiotics, lower airway microbiome, respiratory health

Introduction

Every mammalian body compartment that opens to the outside world has microbial life associated with it[1]. Until recently, the healthy lung was thought to be a sterile environment; however, recent work has demonstrated that the lower respiratory tract is colonized by a complex and roughly stable microbiome that impacts the health of the host[2–4]. For years, the airway microbiota have been theorized to be gatekeepers of respiratory health, as pathogens entering the airway make contact with its microbiota prior to or coincident with their interactions with host cells[3]. While the latter interactions have been studied in detail, little is known about pathogen-microbiome interactions in the airway.

It has been hypothesized that pathogen establishment in the airway could be halted by its microbiota through either indirect or direct competition with the pathogen[3,5,6]. During indirect competition, airway microbiota would modulate the host immune response to increase surveillance, promoting rapid recognition and clearance of foreign microbes including pathogenic organisms. During direct competition, the airway microbiota would competitively exclude a pathogen through production of inhibitory specialized metabolites, and/or by occupying a nutritional niche that would otherwise be used by the pathogen. Enhancement of these defense mechanisms might be achieved through addition of health-promoting microbes (probiotics) directly to the lower airway, an approach that has been demonstrated to prevent pneumococcal and *Pseudomonas aeruginosa* infection previously[7,8].

While these studies have shed light on the utility of lower airway probiotics for preventing two specific infections, greater understanding of the principles that dictate probiotic efficacy would allow rapid identification of probiotics with therapeutic potential against many pathogenic targets. To enable development of these therapies in the future, pipelines for probiotic nomination need to be made which can rapidly and cheaply identify effective therapies. Further, systematic analysis of the mechanism of action of these probiotics would allow fine-tuned control of their activity allowing for more reliable therapeutic outcomes in the clinic.

Here, we seek to fill this gap in knowledge by systematically characterizing factors that make efficacious lower airway probiotics that can competitively exclude a model pathogen, *Burkholderia thailandensis* (*Bt*), from the lung environment. Specifically, we

hypothesize that negative microbial interactions between a probiotic and pathogen better protect the host against infection. Our systematic study of the microbial ecology of these organisms enables development of a pipeline for nomination of effective single and multi-organism probiotics that, to this point, remain underdeveloped. We show that using our pipeline, we can accurately identify pairwise combinations of organisms with enhanced activity against *Bt*. Finally, we test the ability of these prophylactically administered probiotics to promote survival during a challenge with *Bt in vivo*.

Results

Isolation and characterization of candidate probiotics

To develop a system for testing the efficacy of lower airway probiotics in preventing infection, it was first necessary to identify a suitable pathogen to investigate. *Burkholderia thailandensis* (*Bt*) is a pathogen of mice that is genomically similar to several human pathogens including *Burkholderia pseudomallei, Burkholderia mallei* and organisms of the *Burkholderia cepacia complex,* the latter of which poses a high risk of mortality for cystic fibrosis patients[9–13]. Thus, *Burkholderia thailandensis* is an appropriate subject of study for our purposes as it is safe, infectious in mice and a good model of several pathogens with clinical relevance.

To acquire candidate probiotics for use in the lower airway, we sought organisms which would be able to survive in the lower airway for an extended period of time and be capable of tolerating its low-nutrient environment[14]. We hypothesized that organisms directly isolated from the airway would fulfill this criterion, as they are already well-adapted to the environment and may be more immunologically tolerated by the host. To isolate candidate probiotics, the trachea and lungs were collected from C57Bl/6j mice, homogenized, and plated onto five different solid growth media, either directly or after an initial period of culture in blood bottles. Tissues that should be sterile (liver and spleen) were collected from the same mice and processed in parallel, in order to recover any contaminants [“background” (B) strains] inadvertently introduced through our bacterial isolation procedures. Bacterial colonies were repeatedly streaked on LB agar to recover clonal isolates for whole-genome sequencing. In total, 28 isolates recovered from the lower airway tissues were further characterized for use as airway probiotics.

Prior work on the lung microbiome has led to the widely held hypothesis that many of its constituents originate from the oral and/or nasal microbiome and are unable to actively replicate and persist in the lower airway[15,16]. We therefore sought to identify airway isolates that are capable of active growth in the lower respiratory tract, with the

supposition that they should be better equipped to re-colonize the airway and compete against an invading pathogen. To do this, the airway isolates were cultured in lung simulating medium (LSM), which is based on the nutrient composition of sputum samples from cystic fibrosis patients, and therefore is thought to approximate the nutritional environment of the lower respiratory tract[17–20]. We found that 10 of 28 airway isolates tested were capable of robust growth (>1 doubling within 48 hours) in LSM (Figure S1). These 10 isolates, and model pathogen *Bt*, are arrayed on a phylogenomic tree (Figure 1A), and are henceforth referred to as candidate probiotics (CPs).

The phylogenetic assignments of the CPs were compared to those of airway microbiome constituents previously identified through 16S rRNA profiling of mouse airway tissue[21–25]. This analysis revealed that the taxonomic groups to which the CPs belong are well represented in the mouse airway microbiome (Tables S1-3). For example, we found that all 9 of the species to which the CPs belong were detected in at least 1 of 4 previous airway microbiome profiling efforts, with 7 of the 9 species detected in more than 1 profiling effort. In contrast, only 1 of the 9 species to which the B strains (contaminants recovered from liver and spleen) belong was detected, in only 1 of the 4 profiling efforts. Similarly, 3 of the 4 genera to which CPs belong were detected in all 4 profiling efforts (whereas for B strains, only 3 of 9 genera were detected in all 4 efforts); and all 4 of the families to which the CPs belong were detected in all 4 profiling efforts (whereas for B strains, only 6 of 8 families were detected in all 4 efforts). These results indicate that the CPs belong to taxonomic groups that are typically well represented in mouse airway microbiome, consistent with the idea that they are airway microbiome constituents that have been recovered into culture.

Next, we aimed to identify CPs capable of inhibiting *Bt* during co-culture in LSM, with the hypothesis that they might also inhibit *Bt* in the lower respiratory tract and therefore serve as efficacious probiotics. Expression of antagonistic phenotypes is dependent on several factors including the cell density relative to the available resources[26,27]. Accordingly, we decided to assay interbacterial interactions in LSM across varying cell densities, with the hypothesis that this would enable us to capture information about CP potency. Each CP was co-cultured with *Bt* in LSM at different relative ratios (Figure 1B). We found that the CPs showed a range of activities, including negative interactions (Figure 1C top 6 plots) and positive interactions (Figure 1C lower 4 plots) with *Bt*; the potency of each CP, as indicated by IC50 value, is shown in Table 1.

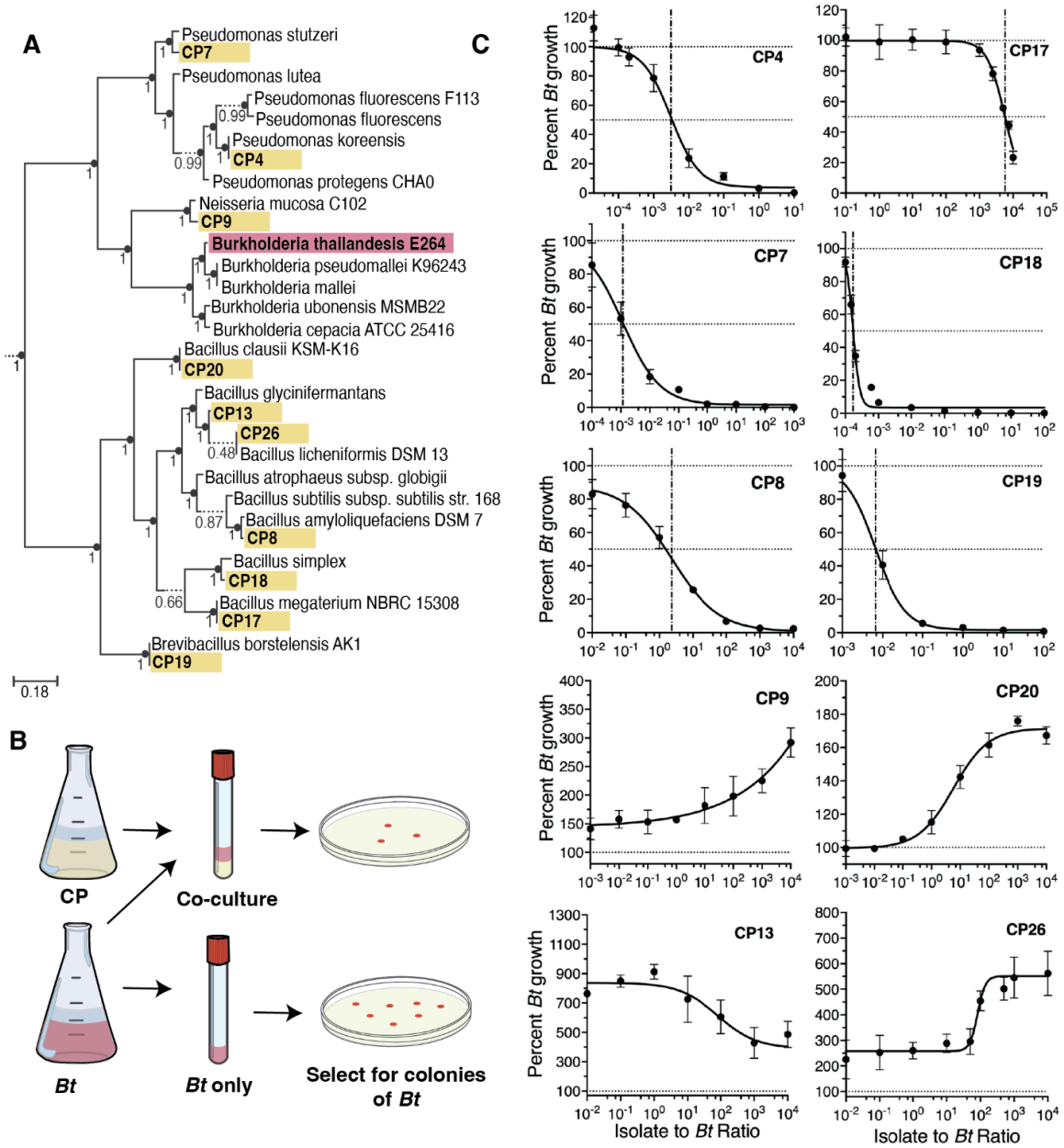

Figure 1 Characterization of CP activity against *B. thailandensis* in vitro. (A) Phylogenomic tree of CPs (yellow) and model pathogen *B. thailandensis* (Bt) (red), interspersed amongst publicly available genomes (no color). (B) Schematic of competition assay used to test in vitro inhibitory capabilities. Percent growth of *Bt* is calculated as the CFU in co-culture at 24 hours divided by the CFU in the *Bt* monoculture at 24 hours multiplied by 100. Co-culture inhibition was tested for multiple starting densities of CP (see Figure 1C x-axis). Starting density of *Bt* and CP at a 1:1 ratio are 3.33x104 CFU/ml per organism. *Bt* monoculture is inoculated at 3.33×10^4 CFU/ml. (C) Dose-response curves for CPs against Bt. Relative IC50 is denoted with a vertical dashed-dotted line, and 100% and 50% growth are denoted with horizontal dotted lines. Percent growth at each density is represented as mean ± SEM.

CP	Species	Relative IC50	95% CI	*Bt* growth at a 1:1 ratio (%)	Niche Index
CP7	*Pseudomonas stutzeri*	0.001172	0.0006442-0.003346	1.893	0.875
CP4	*Pseudomonas fluorescens*	0.003086	0.001791-0.005331	3.200	0.869
CP19	*Brevibacillus borstelensis*	0.006604	0.006484 - 0.01141	3.046	0.775
CP17	*Bacillus megaterium*	5738	3598 – n.d.	98.99	0.704
CP18	*Peribacillus frigoritolerans*	0.0001693	0.0001633 - 0.0001850	0.534	0.591
CP20	*Bacillus clausii*	n.d.	n.d.	115.2	0.457
CP26	*Bacillus licheniformis*	n.d.	n.d.	260.0	0.433
CP13	*Bacillus licheniformis*	n.d.	n.d.	913.0	0.421
CP9	*Neisseria lactamica*	n.d.	n.d.	157.1	0.357
CP8	*Bacillus velezensis*	2.316	0.8280 – 5.073	56.97	0.351

Table 1 Summary of pathogen inhibition by CPs. Relative IC50 values and 95% confidence intervals (95% CI) are shown for each inhibitory CP. Not determined (n.d.) indicates that a value could not be measured. CPs are listed in order of decreasing NI values.

Production of a specialized metabolite plays a role in the antagonistic activities of CP8

Next, we sought to better understand the mechanism(s) of the observed negative interactions. First, we hypothesized that those CPs that strongly inhibit *Bt* may do so by simply growing at a faster rate than the pathogen thus dominating the environment. However, we found no correlation between doubling time of the CPs in LSM and their *Bt* antagonism ($r = -0.21$, $P = 0.155$, 95% CI [-0.47 to 0.088], $N = 49$). It has been shown previously that bacteriophages can modulate interbacterial competition, and some that can target *Bt* have been identified[28–31]; therefore, we next hypothesized that some of the negative interactions between CPs and *Bt* might be mediated through production of *Bt*-targeting phages. To test this, we attempted to recover phages from each CP using standard methods[32,33], and tested the resulting product against *Bt* in plaque assays (Figure S2). We found that none of the CPs appeared to produce a phage that could effectively lyse *Bt*.

Given this information, we next hypothesized that these negative interactions could be direct, through chemical attack (ie. production of inhibitory metabolites); or indirect, through occupying a shared metabolic niche with the pathogen. First, we investigated

the presence of inhibitory metabolites by growing *Bt* in sterilized co-culture supernatant from itself and a CP. We predicted that if *Bt*-inhibiting secondary metabolites were produced by a given CP during co-culture in LSM, then the conditioned medium recovered from the co-culture would inhibit growth of *Bt*. To test this, each negatively-interacting CP was co-cultured with *Bt* for 72 hours, filter sterilized, and combined with double-concentrated LSM to serve as medium for *Bt* growth curves (Figure 2A). We found that the co-culture supernatant from only one of the airway isolates (CP8) significantly reduced growth of *Bt* compared to supernatant from a *Bt* monoculture (negative control) (Figure 2B). This indicated that CP8 likely produced a specialized metabolite and was engaging in interference competition. To confirm our findings, we performed agar diffusion assays on all inhibitory CPs and found that, aside from CP8, none produced a zone of inhibition on a lawn of *Bt* (data not shown).

To understand the degree to which CP8's secondary metabolite is responsible for mediating the competitive phenotype observed in Figure 1C, we aimed to create a knockout of this molecule in CP8. Previously, we used antiSMASH[34] to identify biosynthetic gene clusters in the CP8 genome sequence, and found that CP8 likely produces 19 specialized metabolites[35]. A review of the literature revealed that biosynthesis of many of these specialized metabolites is dependent on Sfp, a phosphopantetheinyl transferase which catalyzes their conversion to the active holo-form[36–39]. Therefore, we hypothesized that knocking out the *sfp* gene in CP8 would yield a mutant with an inability to produce a specialized metabolite with inhibitory capabilities against *Bt*. A clean deletion of the *sfp* gene was made in CP8, and the resulting mutant (CP8Δ*sfp*) was found to produce a smaller zone of inhibition in an agar diffusion assay, indicating that interference competition was reduced (Figure 2C). Additionally, growth curves of wildtype CP8 and the CP8Δ*sfp* mutant were performed, which showed no growth defect in the mutant strain (Figure 2D), indicating that its reduction in interference competition was not due to a growth defect. Finally, a competition assay was performed using the CP8Δ*sfp* mutant. The mutant showed reduced inhibitory activity compared to wildtype CP8 and, in contrast, demonstrated a positive interaction with *Bt* when interference competition was disrupted (Figure 2E).

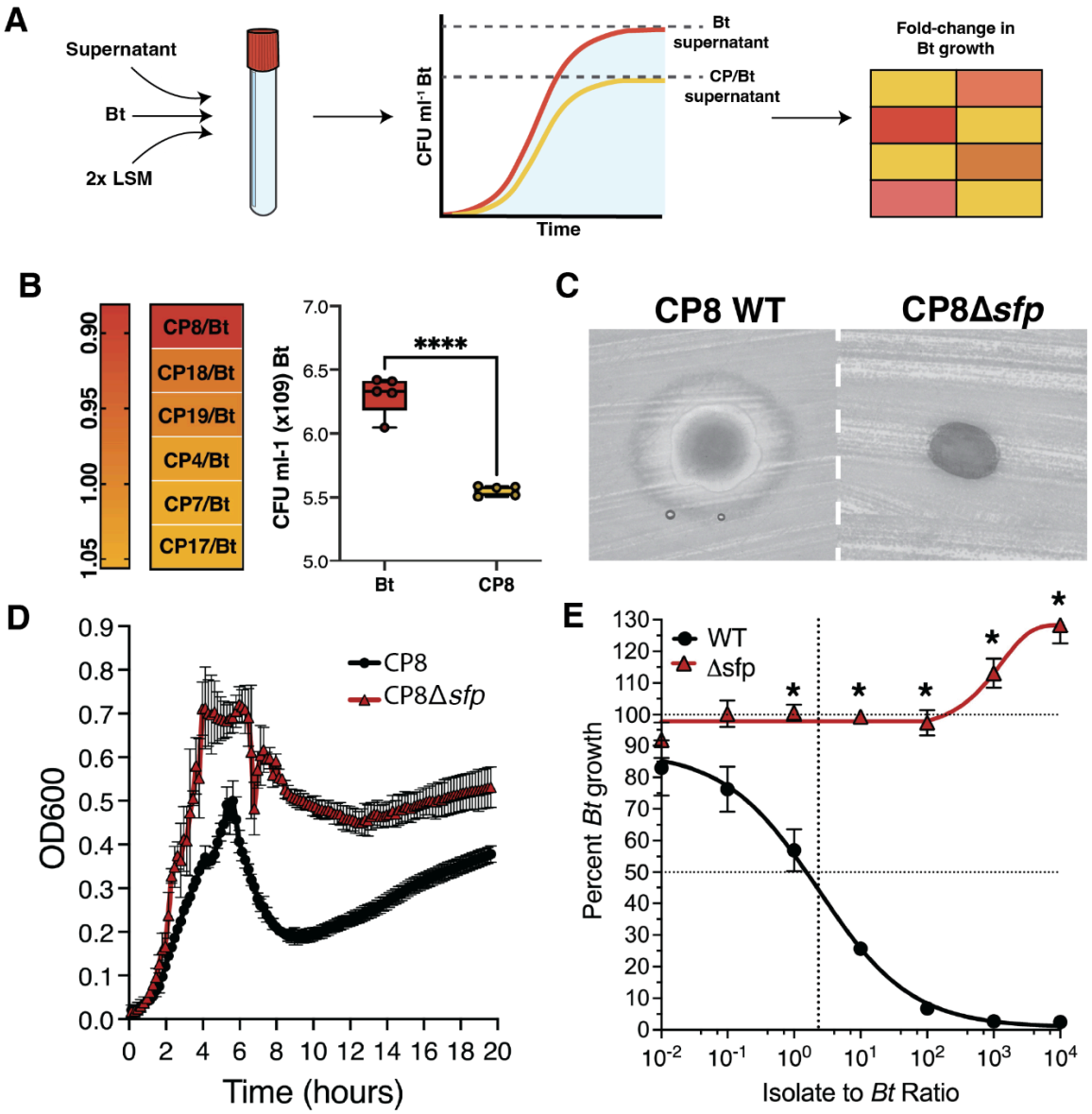

Figure 2 Production of a specialized metabolite plays a role in the antagonistic activities of CP8. (A) Schematic representation of supernatant inhibition experiment workflow. Supernatant from a *Bt* and CP co-culture or from *Bt* monoculture (supernatant) is mixed 1:1 with 2x LSM. This mixture is used as the growth medium for subsequent *Bt* growth curves. Fold-change in *Bt* growth is calculated by dividing the maximum growth of *Bt* in co-culture supernatant by the maximum growth of *Bt* grown in supernatant from itself. (B) Left: Heatmap of fold-change in max CFU of *Bt* grown in supernatant from each inhibitory CP and *Bt* co-culture relative to *Bt* grown in supernatant from itself. Co-culture supernatant was collected at 72 hours. A fold-change of 1 indicates no difference in growth in co-culture supernatant compared to *Bt* growth in supernatant from itself. A fold-change less than 1 indicates a reduction in pathogen growth. Right: Boxplot of growth inhibition by CP8 supernatant. Data are represented as mean ± SD. (C) Agar diffusion assays testing the CP8 wildtype strain (CP8 WT) and sfp mutant strain (CP8Δsfp) for inhibition of Bt after 48 hours. (D) Growth curves of CP8 WT (black) and CP8Δsfp (red) (E) Dose-response curve of CP8 WT (black) and CP8Δsfp (red) against Bt after 24 hours of co-culture. Percent growth at each density is represented as mean ± SEM.

Metabolic niche overlap is indicative pathogen and CP antagonism

While production of an inhibitory metabolite appeared to be the primary mode of inhibition for CP8, 5 other CPs showed a negative interaction with *Bt* but did not appear to produce specialized metabolites. Previous work has shown that competition for a shared metabolic niche is an important mediator of interbacterial interactions in bacterial communities[40–44]. Therefore, we hypothesized that inhibition of *Bt* by these 5 CPs may be due to metabolic niche overlap. Specifically, we postulated that passive consumption of a limiting resource by the CP could reduce the supply to *Bt,* thus inhibiting its growth.

The Redfield Ratio describes the stoichiometric relationship between carbon, nitrogen and phosphorus which supports life on earth and is canonically 106:16:1[45]. Recent work has shown that this ratio is variable across body sites, with areas like the mouth and gut being more carbon rich, and the airways being relatively carbon poor[46]. Similar to the upper airway, LSM is carbon limiting, with a C:N:P ratio of approximately 88:14:1. This suggests that carbon may be the limiting nutrient in the lower airway and thus, may be the limiting resource in the airway niche. We predicted that if carbon was limiting, then supplementation of LSM with additional carbon would reduce the antagonism between the CP and *Bt*. To test this, LSM was supplemented with 43mM glucose to increase the C:N:P ratio to 101:14:1. We observed a leftward shift of the dose-response curve for CP7 in the additional carbon condition (Figure 3A), and a significant reduction in inhibition at a 1:100 ratio (Figure 3B). A similar result was observed when the same experiment was conducted with CP19 (Figure S3). These results suggest that with increased carbon abundance there is a reduction in antagonism, consistent with the idea that, under the carbon limiting conditions of the airway, carbon is the primary nutrient for which CPs and *Bt* are competing.

Further, we sought to explore the extent to which metabolic overlap with *Bt* for carbon sources could predict inhibitory capabilities of each CP. To do this, we assayed the growth of each CP and *Bt* in each individual carbon source from LSM to determine which carbon sources could be utilized by each organism (Figure 3C). *Bt* showed a wide range of metabolic potential and was able to grow on every carbon source presented except for ornithine. This is perhaps unsurprising as it has been shown previously that pathogens acquire new metabolisms in order to survive in their host[47]. Conversely, the CPs displayed diverse metabolic activity, with CP4 and CP7 appearing most similar to *Bt* (Figure 3C).

Each carbon source in LSM is used both for production of biomass as well as the primary electron donor to generate energy via aerobic respiration. In the niche exclusion

hypothesis, a competitive advantage can be obtained for an organism that is able to consume those resources that would otherwise fuel aerobic respiration of a competitor. We therefore hypothesized that those CPs that are capable of sharing a greater proportion of carbon-derived electrons with *Bt* would have more potent antagonism of the pathogen by covering a greater percentage of the energetic niche (Figure 3D). On this assumption, we built a simple index of niche overlap which weights each carbon source in LSM utilized by a given CP by the theoretical electron contribution of that given source, with the belief that such a metric could identify probiotics capable of achieving maximal niche coverage. We hypothesized that weighting each carbon source by its theoretical electron contribution would improve the accuracy of the niche index, as those sources which contribute more electrons represent a greater proportion of the energetic niche and therefore have a potentially greater impact on antagonistic phenotypes. Niche Index (NI) is calculated as follows:

First, the number of electron equivalents generated by each carbon source is calculated assuming the complete oxidation of these sources to carbon dioxide under standard conditions. The electron equivalents are then multiplied by the total number of molecules of the carbon source in the media. This yields the total electron equivalents for each carbon source per liter of media. These values are held in vector $\vec{E}$.

$$\vec{E} = \begin{pmatrix} glucose \\ lactate \\ asparticacid \\ threonine \\ serine \\ glutamine \\ proline \\ glycine \\ alanine \\ cysteine \\ valine \\ methionine \\ isoleucine \\ leucine \\ tyrosine \\ phenylalanine \\ ornthine \\ lysine \\ histidine \\ tryptophan \\ arginine \end{pmatrix} = \begin{pmatrix} 8.02 \times 10^{22} \\ 6.72 \times 10^{22} \\ 5.98 \times 10^{21} \\ 1.03 \times 10^{22} \\ 8.71 \times 10^{21} \\ 1.68 \times 10^{22} \\ 2.20 \times 10^{22} \\ 4.35 \times 10^{21} \\ 1.29 \times 10^{22} \\ 1.54 \times 10^{21} \\ 1.61 \times 10^{22} \\ 1.07 \times 10^{22} \\ 2.02 \times 10^{22} \\ 2.91 \times 10^{22} \\ 1.84 \times 10^{22} \\ 1.28 \times 10^{22} \\ 8.96 \times 10^{21} \\ 3.59 \times 10^{22} \\ 6.25 \times 10^{21} \\ 3.60 \times 10^{20} \\ 4.05 \times 10^{21} \end{pmatrix}$$

The weighted value for each carbon source is:

$$\overrightarrow{W} = \frac{\vec{E}}{E_{glucose}} \tag{1}$$

For all CPs and *Bt*, a carbon utilization vector is generated. If a carbon source is consumed, then i = 1, if it is not able to be consumed, then i = 0.

$$\overrightarrow{CU_{CP}} = \begin{bmatrix} i_1 \\ i_2 \\ i_3 \\ i_4 \\ \vdots \\ i_n \end{bmatrix},$$

To calculate the Niche Index of each CP with *Bt*, the Hadamard product of the carbon utilizations vectors for each CP and *Bt* are multiplied by the weighting vector. The resulting value represents the electron equivalents utilized by both the CP and *Bt*. This value is divided by the electron equivalents utilized by *Bt* alone. Thus, the equation for Niche Index is: :

$$NI_{CP} = \frac{[\vec{CU}_{CP} \odot \vec{CU}_{Bt}] \cdot \vec{W}}{[\vec{CU}_{Bt} \cdot \vec{W}] - [CU_{CP,orn} \cdot W]} \qquad (2)$$

NI is higher when a given CP shares a greater number of carbon-derived electrons with *Bt.* To evaluate the association between the co-culture interaction with *Bt* and the NI of each CP, a non-parametric spearman rank-order correlation was performed with the null hypothesis that there is no monotonic association between the two variables. We found that NI is negatively associated with the co-culture growth of *Bt* with a given CP at a 1:1 ratio ($r = -0.64$, $P < 0.0001$, 95% CI [-0.79 -0.43], $N = 49$) (Table 1 and Figure 3E). Since CP8's potency is primarily due its secondary metabolite production (Figure 2E), percent growth of the pathogen in co-culture with the CP8Δ*sfp* mutant was used in this analysis to understand how NI relates to CP8's interaction with *Bt* (Figure 3E). While here we have used Niche Index to calculate niche overlap between CPs and *Bt* in LSM, this model is generalizable and can be used to calculate the niche overlap between organisms in any media with a known molar carbon composition.

To confirm our hypothesis that those organisms that consume a greater number of carbon-derived electrons with *Bt* are more antagonistic, we performed exometabolomics on supernatants from 3 CPs. These 3 CPs represent a range of inhibition strengths and

niche indexes, with CP7 being the most potent (IC50 = 0.001172 NI = 0.875), CP19 displaying moderate potency (IC50 = 0.006604 NI = 0.775) and CP8 being the least potent (IC50 = 2.316 NI = 0.351). Each of these CPs was combined with *Bt* at their respective IC90 and co-incubated for 36 hours. Supernatants from these CPs at 36 hours show that more potent CPs consume a statistically greater amount of carbon from the media than less potent CPs (Figure 3F). At 24 hours where the degree of inhibition of *Bt* by each CP is the same, more potent probiotics consume fewer carbon-derived electrons than less potent competitors (Figure 3G). This led us to hypothesize that certain carbon sources were being prioritized, allowing more antagonistic CPs to have the same net effect on *Bt* while consuming fewer electrons. Further, we speculated that if high priority carbon sources were to be identified, perhaps the consumption of a smaller set of these high priority carbon sources could predict activity with similar accuracy to the Niche Index.

From the exometabolomics data, consumption of three carbon sources, lactate, proline and aspartic acid are prioritized more at 24 hours by the most potent candidate probiotic, CP7, than the least potent, CP8 (Figure 3H). Furthermore, we found that a CP's ability to generate biomass on lactate (the second most abundant carbon source in LSM) was a good predictor of its ability to inhibit the pathogen (Figure 3I), suggesting that the ability to consume lactate in co-culture may be important for pathogen control. Overall, these results indicate that consumption of specific resources can have an especially strong influence on niche exclusion, with consumption of a specific carbon source (lactate) appearing to play a key role in niche exclusion of *Bt* by the most potent of the CPs (CP7). While these results are promising building blocks for the development of a metric of activity based upon a smaller feature set, a larger screen of candidate probiotics may be necessary to understand the generalizability of these features. Further, future efforts to develop this model should take into account a CP's uptake rate for a given resource as this may influence antagonism and reveal features of the metabolic niche that have disproportionate significance to interbacterial interactions.

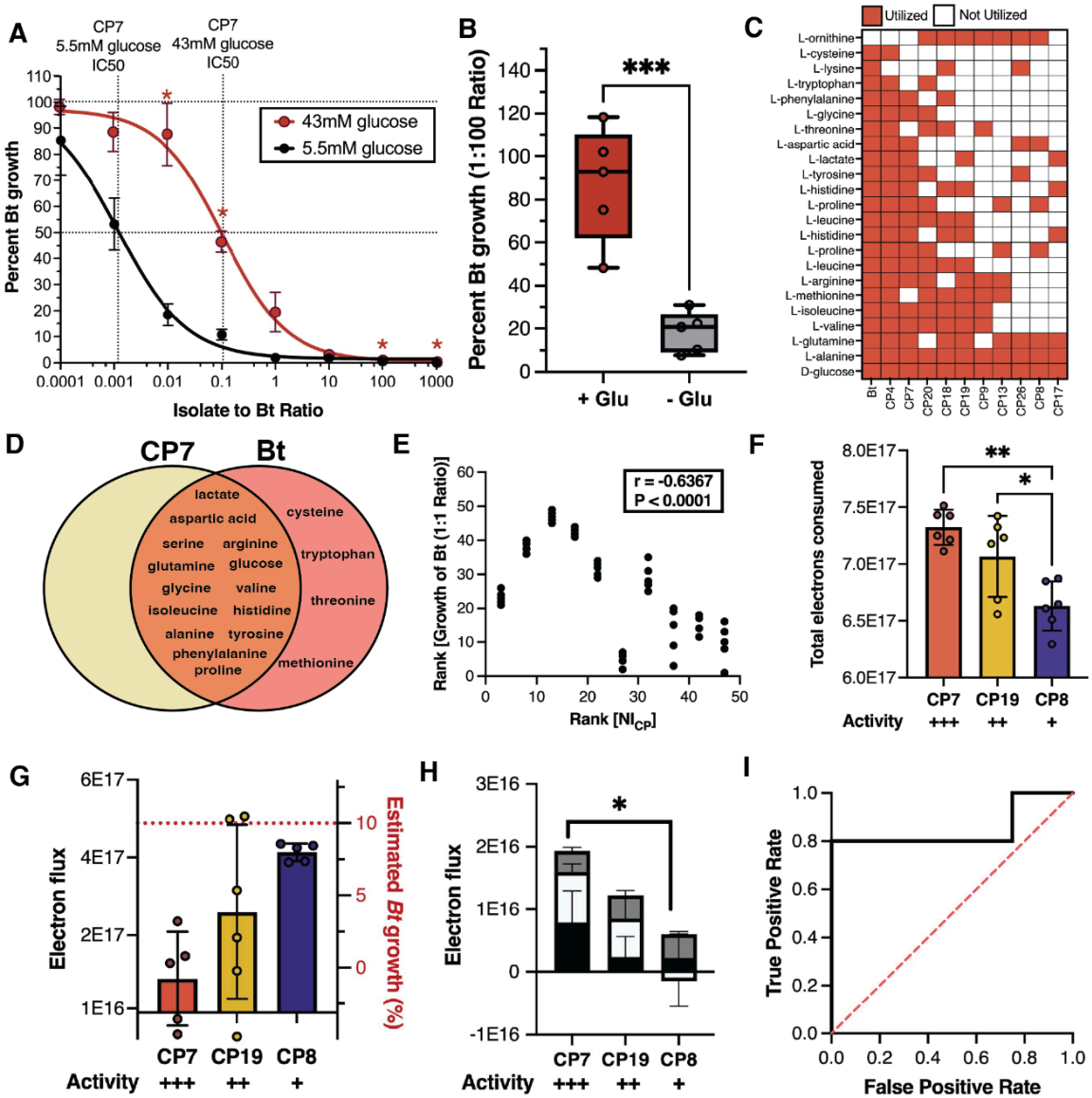

Figure 3 Metabolic niche overlap is indicative of pathogen and CP antagonism. (A) Dose-response curve for CP7 grown in unsupplemented LSM (black) or with additional glucose (red). Percent growth at each density is represented as mean ± SEM. (B) Activity of CP7 against Bt at a 1:100 ratio with or without glucose supplementation (red and gray, respectively). Data are summarized as mean ± SD. ***P<0.001. (C) Carbon utilization heatmap for CPs and Bt. (D) Venn diagram of carbon sources utilized by CP7 and Bt. (E) Plot of rank percent *Bt* growth at a 1:1 ratio after 24 hours vs rank of Niche Index for each CP. Correlation is determined by Spearman rank correlation (r = -0.6367, P < 0.0001, 95% CI [-0.7891 -0.4261], N = 49). (F) Total carbon consumed by CPs grown in combination with Bt at 36 hours (mean ± SD). Activity indicates relative amount of Bt inhibition at a 1:1 ratio from most (+++) to least (+) inhibitory. *P=0.05; **P<0.01. (G) Total electron flux at 24 hours. Red dashed line indicates the estimated abundance of *Bt* in each co-culture. (H) Summed electron flux of lactate (black), proline (white), and aspartic acid (gray) at 24 hours in different CP co-culture conditions (mean ± SD). *P<0.05.(I) Receiver operator characteristic curve showing the ability of growth on lactate to distinguish inhibitory CPs from non-inhibitory CPs. An AUROC of 1 indicates perfect distinction between inhibitors and non-inhibitors; an AUROC of 0.5 (dashed red line) indicates no distinction between inhibitors and non-inhibitors.

Niche overlap aids in the identification of efficacious multi-organism probiotics

While our work showed that 6 of the CPs were potent inhibitors of *Bt* growth in co-culture, 4 were poor inhibitors or actually promoted *Bt* growth (Figure 1). Having found that NI is well correlated with CP activity *in vitro*, we hypothesized that this metric could be altered to identify pairwise combinations of poor-performing CPs with enhanced antagonism. To do this, we created a new metric, the Niche Index Fraction (NIF), which is calculated by generating the NI between two CPs and dividing this value by the NI of the two CPs and *Bt* (Figure 4A). We hypothesized that combinations with lower NIF values would have optimal coverage of the *Bt* niche space while minimizing niche overlap between two CPs. Thus, low NIF values might indicate combinations with enhanced inhibition of the pathogen compared to each CP alone. NIF is calculated as follows:

First, the overlap between two CPs is generated and is weighted by the relative electron contribution of each carbon source

$$y = [\vec{CU}_{CPx} \odot \vec{CU}_{CPy}] \cdot \vec{W} \tag{3}$$

Total carbon-derived electron utilization is calculated for both CPs

$$p = \vec{X}_{CPx,CPy} \cdot \vec{W}, \textit{such that } p \textit{ is never } 0 \tag{4}$$

For which

$$\vec{X}_{CPx,CPy} = \begin{cases} \vec{X}_{CPx,CPy} = 1 \text{ if } \overrightarrow{CU}_{i,CPx} = 1 \text{ and } \overrightarrow{CU}_{i,CPy} = 1 \\ \vec{X}_{CPx,CPy} = 0 \text{ if } \overrightarrow{CU}_{i,CPx} = 0 \text{ and } \overrightarrow{CU}_{i,CPy} = 0 \\ \vec{X}_{CPx,CPy} = 1 \text{ if } \overrightarrow{CU}_{i,CPx} \neq \overrightarrow{CU}_{i,CPy} \end{cases} \tag{5}$$

Thus the niche overlap between two CPs is

$$NI_{CPx,CPy} = \frac{y}{p} \tag{6}$$

The niche overlap between two CPs and *Bt* is thus

$$NIF_{CPx,CPy} = \frac{NI_{CPx,CPy}}{[C\vec{U}_{Bt} \cdot \vec{W}] - [\vec{X}_{CPx,CPy,orn} \cdot \vec{W}]} \tag{7}$$

We calculated NIF for every pairwise combination of the 7 least antagonistic CPs from Figure 1. This generated a matrix of CP combinations and their respective NIF values (Figure 4B). To test this metric's capability to identify inhibitory combinations of CPs, we chose to evaluate pairwise combinations with the three lowest NIF values, a moderate value and a high value using competition assays.

In these experiments, two CPs were combined at a 1:1 ratio such that the total CP concentration at a given ratio was the same as their individual CP counterparts. This enabled us to directly compare activity of an individual CP and the activity of a combination of two CPs at a given ratio as the total cell density was the same in each. From competition assays, we determined that NIF was able to predict combinations with enhanced and reduced *Bt* antagonism as reflected by their relative IC50 values (Figure 4C,D,E, Figure S4 and Table S4).

For one combination, CP8 and CP19, we sought to understand the mechanism by which antagonism was being enhanced. First, to understand the effect of the interaction on all members of the co-culture, we performed growth curves of each strain (CP8, CP19 and *Bt*) in co-culture and compared their individual abundances when grown together to their growth in monoculture using qPCR (Figure S5). Reduced growth in co-culture of all three organisms in comparison to monoculture (Figure S1) classifies this antagonistic interaction as true competition. To better understand how CP8 and CP19 may enhance each other's antagonistic impact on *Bt*, we performed exometabolomics analysis on supernatant from this combination. At 24 hours, significantly more lactate was consumed per cell by the CP8/CP19/*Bt* co-culture than by the CP8/*Bt* co-culture or CP19/*Bt* co-culture ($p<0.0001$) (Figure 4F). Similarly to the single isolate studies, this result once again suggests that lactate utilization may be important for antagonism of *Bt* in an airway-simulating environment.

To further investigate how the combination of CP8 and CP19 more effectively inhibits the pathogen, we performed a competition assay using the CP8Δ*sfp* mutant in combination with CP19 to understand the degree to which secondary metabolite production was responsible for their combined effect (Figure 4G). When wildtype CP8 was replaced with the CP8Δ*sfp* mutant, there was a significant reduction in *Bt* inhibitory activity compared to the wildtype CP8/CP19 combination. Together, these findings suggest that both consumption of specific carbon sources and secondary metabolite production are important for activity of the CP8/CP19 combination and likely enable *Bt* inhibition activity (Figure 4H). While the concept of NIF suggests that coverage of the pathogen niche may be responsible for the observed activity in other combinations, further investigation needs to be done to understand these interactions in more detail.

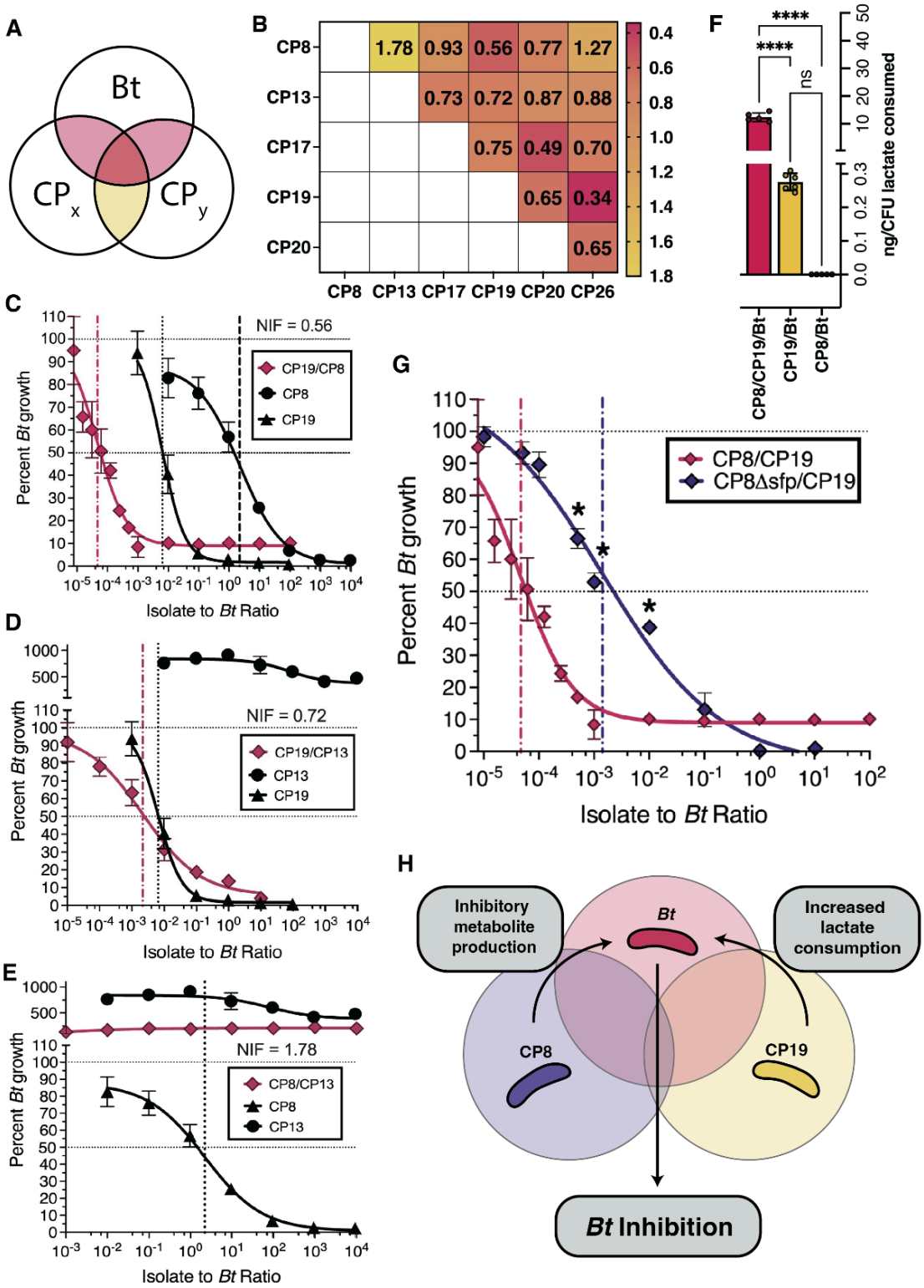

Figure 4 Niche overlap aids in identification of efficacious CP combinations. (A) Venn diagram representation of the Niche Index Fraction (NIF) calculation. Yellow represents the fraction numerator and red the denominator. (B) Heatmap of NIF values for each colonizing CP. (C) Dose-response curve for the CP8/CP19 combination (mean ± SEM). (D) Dose-response curve for the CP19/CP13 combination (mean ± SEM). (E) Dose-response curve for the CP13/CP8 combination (mean ± SEM). (F) Lactate consumed (as determined via GC-TOF) for 3 conditions, normalized to CFU of each CP inoculated (mean ± SD). ****P<0.0001. (G) Dose-response curve for the CP8/CP19 (red) and CP8sfp/CP19Δsfp (black) combinations. (H) Schematic of the proposed mechanism for *Bt* inhibition by the CP8/CP19 combination. CP8 produces a specialized metabolite that inhibits growth of the *Bt*. Additionally, increased lactate consumption by CP19 in the presence of CP8 further reduces *Bt* growth. Overall, minimal niche overlap between the CPs, and high overlap with *Bt*, allows for further inhibition of *Bt* with minimal inter-CP antagonism.

CPs provide protection against infection

Having observed the ability of the CPs to compete with *Bt* in an *in vitro* airway-simulating environment, we were encouraged to test their ability to confer protection against respiratory *Bt* infection *in vivo*. Firstly, we hypothesized that those CPs which colonized at high density over an extended period of time would provide better protection against *Bt* infection. To test the airway colonization capabilities of the CPs, we administered each to C57Bl/6j mice at 10^6 CFU via oropharyngeal aspiration (OPA). After a period of 7 days, the lungs and trachea were assessed for CP load via CFU enumeration (Figure 5A). We found that several CPs were able to colonize the airway for the duration of the 7-day period (Figure 5B). We were particularly interested in those CPs displaying airway colonization (mean airway CFU load of >10 CFU), as these would seem most likely to be capable of protecting against respiratory *Bt* infection.

We screened both colonizing and non-colonizing CPs for their ability to confer protection in a mouse model of respiratory *Bt* infection. In these studies, 10^6 CFU of each of 6 CPs was administered to the airway of C57Bl/6j mice via OPA. Following a period of 3, 5, or 7 days, *Bt* was administered to the airway and mortality was monitored for 10 days following *Bt* challenge (Figure 5C). Mice administered no CP prior to *Bt* challenge showed high mortality, only rarely surviving past day 4 (Figure 5D). In contrast, mice administered certain CPs prior to *Bt* challenge showed significantly reduced mortality (Figure 5D). Five of the six CPs were protective when administered 3 days prior to *Bt* challenge; CP17 was protective when administered at 3 or 5 days prior to *Bt* challenge; and CP19 was protective when administered at 3, 5, or 7 days prior to *Bt* challenge.

We observed that the most protective probiotics, CP19 and CP17, were predicted to have the highest niche overlap with *Bt* via their NI values and also showed an ability to inhibit in competition assays (Figure 1C). Furthermore, the CPs that did not inhibit *Bt* in competition assays yet do robustly colonize (Figure 5B) (i.e. CP13, CP20, and CP26) showed no significant protection when administered 5 or 7 days prior to *Bt* challenge (Figure 5D). A notable exception to this trend was CP8, which showed inhibition in competition assays as well as robust colonization, but showed no significant protection of mice challenged with *Bt*. This suggests that niche overlap with the pathogen may be more predictive of the protective capabilities of a probiotic than secondary metabolite production.

Finally, we sought to understand if NI_{CP} was related to CP protection efficacy. To test this, we performed a non-parametric spearman rank correlation analysis with the null hypothesis that there existed no relationship between the number of days surviving after pathogen exposure and NI_{CP} when CP treatment was performed 3, 5 or 7 days in advance of infection. We found a moderate relationship between survival and NI_{CP} when CPs are dosed 3 days prior to infection ($r = 0.48$, $P<0.0001$, 95% CI [0.33 to 0.62], $N = 115$), a very strong relationship when dosed 5 days prior ($r = 0.77$, $P<0.0001$, 95% CI [0.60 to 0.88], $N = 40$) and a strong relationship when dosed 7 days prior ($r = 0.66$, $P<0.0001$, 95% CI [0.52 to 0.77], $N = 89$) (Figure 5D). Interestingly, those CPs (ie. CP13, CP20 and CP26) which do not show inhibition in competition experiments (Figure 1C) conferred a significant survival benefit only when administered 3 days prior to infection. This suggests an alternative mechanism of protection at this timepoint which our model does not capture, such as competition for resources other than carbon (eg. other nutrients) or immune priming. While it appears that NI is a reasonable indicator of the protective effects of a CP *in vivo*, additional development of this model will need to be done to better capture the host environment, improve prediction and determine the extent to which it can be used to nominate efficacious probiotics in the future.

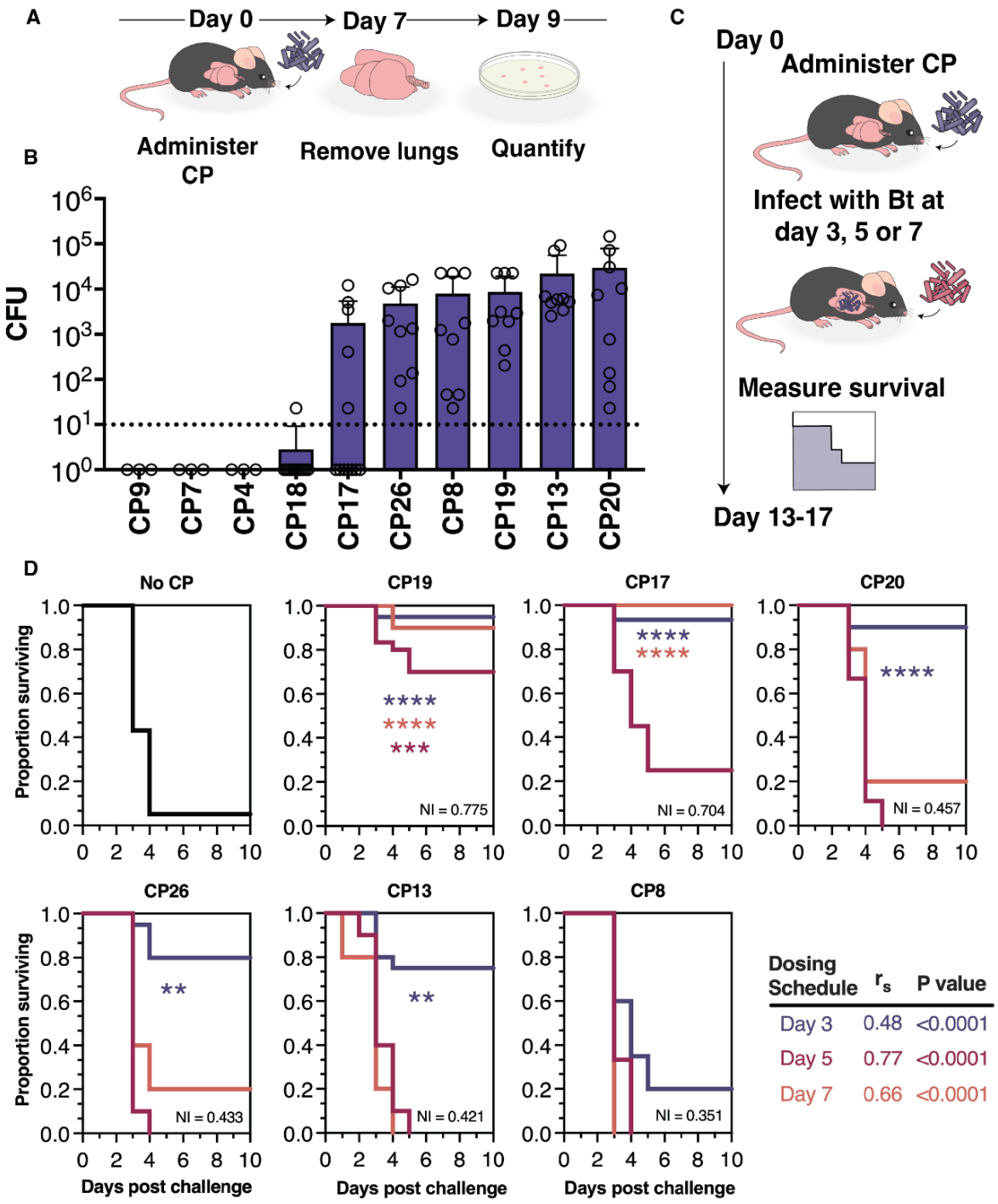

Figure 5 CPs colonize the mouse airway, and protect against respiratory *Bt* infection. (A) Schematic of colonization testing for CPs. Each CP (10^6 CFU) is administered to the lower airway via OPA.. After 7 days, the airway tissues (lungs and trachea) are collected, homogenized, and plated in order to enumerate viable CPs (expressed as CFU per tissue homogenate). (B) Colonization results from airway tissues collected at 7 days following CP administration. The dotted line represents the minimum CFU at which the CP is considered able to colonize in a reliably detectable manner. Data are represented as the mean ± SD. (C) Schematic of the method for survival testing. Each CP (10^6 CFU) is administered to the lower airway via OPA; and then, at 3, 5, or 7 days post-CP, challenged with a normally lethal dose of *Bt* ($3x10^4$ - $5x10^5$ CFU). Survival is measured over the course of 10 days post-*Bt*. (D) Survival data from mice administered no CP (vehicle control), CPs at 3 days (blue), 5 days (orange), or 7 days (red) prior to *Bt* challenge. The Niche Index value for each CP is listed in the lower-right corner of its associated graph. Comparison of survival rate with versus without CP treatment was accomplished using the Mantel-Cox test ****P<0.0001, ***P<0.0002, **P<0.01. A summary of the relationship between days surviving and Niche Index value for each dosing schedule is also shown.

Discussion

The human respiratory tract microbiome composition has been linked to both respiratory health and the occurrence of respiratory infections[54]. As a result of this connection, manipulation of the lower airway microbiome is an attractive strategy for anti-infective therapies. Airway microbiome modulation via supplementation with probiotics has previously shown success in preventing infections; however, these studies lack a more broad and systematic analysis which is necessary to learn generalizable principles for the design of efficacious airway probiotics[7,8].

In this work, we developed a system that probes interactions between airway-derived candidate probiotics (CPs) and a model respiratory pathogen *Burkholderia thailandensis* (*Bt*). From this exploration, we find that consumption of shared resources explains the majority of antagonistic phenotypes between CPs and *Bt in vitro*. Specifically, consumption of shared carbon sources seems to play an important role in these interactions. As a result, a metric of niche overlap, Niche Index (NI), is correlated with CP inhibitory activity *in vitro* in most instances. Furthermore, we use these same principles to design combinations of CPs with enhanced antagonism against *Bt*. We explore the mechanism by which one combination, CP19 and CP8, exploits both metabolic niche exclusion and inhibitory metabolite production to its advantage in competing with *Bt*. Finally, we find that several CPs are able to re-colonize the mouse airway for at least 7 days, and that two CPs (CP19 and CP17) significantly reduce mortality in mice subjected to otherwise lethal respiratory *Bt* challenge. While it appears that there is a relationship between the NI and the protective capabilities of a CP, further preclinical experiments will need to be done to determine if NI alone can guide formulation of airway probiotics with clinical applicability. Further, consideration of potential effects from patient genetic background, environment, host immune response, and cross-feeding must also be explored.

The method described here is a step towards a more rapid, inexpensive, and effective means of identifying efficacious probiotics, all factors that have stalled probiotic development previously[55]. Selection of these probiotics based on their niche-exclusion capabilities, as demonstrated here, also has the potential to enable development of probiotics with better safety profiles. While probiotics with the ability to produce inhibitory small molecules can be identified easily, pathogens can rapidly evolve to evade this form of antagonism. In comparison, probiotics which occupy a niche may leave a pathogen with fewer strategies to evolve resistance, allowing long-term efficacy and more predictable effects on health in clinical applications.

Another great challenge for clinical development of airway probiotics is potency. In order to allow for adequate oxygen exchange in the lungs, alveoli need to remain unobstructed and, thus, colonization of the lung with a large dose of bacteria may result in undesirable outcomes. Therefore, probiotics which require extremely low doses to achieve a protective effect are desirable. Our methodology shows potential for repurposing of organisms that are typically poor performers for use in highly potent multi-organism formulations.

In this work, we found that one way that multi-organism probiotics defend against a pathogen is through consumption of available carbon sources which would otherwise feed the pathogen. In particular, lactate consumption appears to be important for efficacy. Several studies have found that there is increased lactate in the lung during inflammatory exacerbations, which could feed pathogen growth[56–58]. Interestingly, previous studies have shown that consumption of lactate is important for fitness in the host and pathogenesis for several different bacterial pathogens[59–63]. Theoretically, if probiotics that preferentially consume lactate can be designed, they may be useful in controlling infections in hosts with inflammatory lung conditions, such as cystic fibrosis, idiopathic pulmonary fibrosis, and chronic obstructive pulmonary disease[57,58,64].

Broadly, we hypothesize that airway probiotics may have functionality by stopping the positive feedback loop of infection. In this model, pathogen infiltration into the lung and growth results in inflammation and cellular injury, causing a leak of nutrient-rich fluids into the alveolar compartment, which further promotes pathogen growth (Figure 6 (left))[15]. Airway probiotics might stop this feedback loop by depleting nutrient abundance in the local lung environment, thereby limiting pathogen growth (Figure 6 (right))[15]. Given this model, probiotics which interfere with pathogen metabolism could be forward-designed to work optimally within these environments in order to maximize potency and efficacy.

The native airway microbiome, and its interactions with host cells and incoming pathogens, is only partially understood, making development of airway probiotics a challenge. As our knowledge grows, health-promoting functionalities could be introduced into the lower respiratory tract, through supplementation with microbiome constituents in unaltered state (as demonstrated here) or with engineered properties, such as novel metabolisms. However, for utility in the clinic, numerous questions will need to be answered about the predictability, long-term safety and reliability of airway probiotics as alternatives or additions to antibiotic therapies. To improve this nomination pipeline further, future models should incorporate elements which have been shown to influence interbacterial antagonism previously such as the rate of consumption of shared resources and and the impact of sudden alterations in resource availability as

might occur in acute lung injury. To ensure safety, evolution of the CP in the airway should be monitored over time, and the potential contribution of cross-feeding between CP and pathogen should be investigated. Additionally, future efforts will need to focus on reliable probiotic delivery modalities, formulation stability, and potential for variance in colonization, protection, and immunogenic responses in different hosts and environmental contexts. Work is currently underway to understand the generalizability of the findings here to models of other respiratory diseases, and to evaluate their safety and efficacy for therapeutic applications.

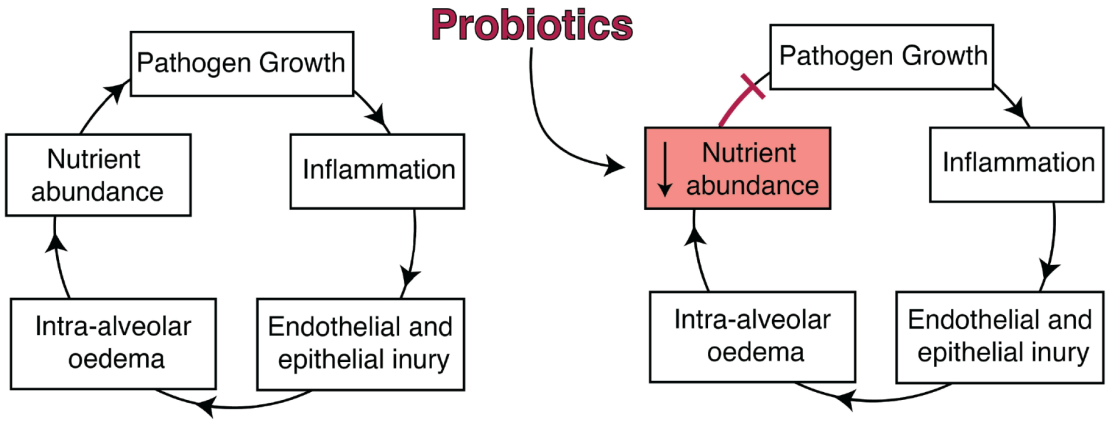

Figure 6 Proposed mechanism of CP protection. Left: During lower airway infection, bacterial growth elicits inflammation from the host, with concurrent endothelial and epithelial injury. Intra-alveolar oedema introduces additional nutrients from the blood into the alveoli and lung lumen, enabling further growth of the pathogen. This positive feedback loop results in uncontrolled growth of the pathogen, ultimately facilitating its instantiation. Right: Probiotics delivered directly to the lower airway may limit infection by reducing nutrient abundance after oedema, which prevents further growth of the pathogen and thereby breaks the infection-promoting feedback loop.

Acknowledgements

We thank K. Sander (UCB) and K. Vyas (CMS) for helpful discussion; D. Sivanandan (UCB) for assistance with experiments; and M. Hirakawa (SNL) for critical review of the manuscript. We thank the West Coast Metabolomics Center for exometabolomics services. Sandia National Laboratories is a multimission laboratory managed and operated by National Technology & Engineering Solutions of Sandia, LLC, a wholly owned subsidiary of Honeywell International Inc., for the U.S. Department of Energy's National Nuclear Security Administration under contract DE-NA0003525.

Author Contributions

Conceptualization, K.E.H., S.S.B. and A.P.A.; Methodology, A.M.P., N.M.C., K.E.H. and H.K.K; Investigation, A.M.P, N.M.C., S.S.B., K.E.H. and H.K.K.; Formal analyses - C.M.M., K.P.W., K.P., S.S.B., A.S., and K.E.H.; Writing – Original Draft, K.E.H.; Writing - Review & Editing, all authors; Funding acquisition, S.S.B. and A.P.A; Supervision, S.S.B. and A.P.A.

Declaration of Interests

K.E.H., S.S.B and A.P.A are listed as inventors on a patent application related to the content of this work.

Methods

Isolation and Culture of Bacteria

A *Burkholderia thailandensis* E264 strain that constitutively expresses GFP was provided by Daniel J. Hassett (University of Cincinnati College of Medicine; Cincinnati, OH)[65]. The candidate probiotic (CP) isolates were recovered from the lower respiratory tracts of healthy mice using a culturomics approach[66]. All animal work was conducted in accordance with protocols approved by the Lawrence Livermore National Laboratory (LLNL) Institutional Animal Care and Use Committee (IACUC, protocol 304) and Institutional Biosafety Committee (IBC, protocol 2021-010). LLNL is accredited by the Association for Assessment and Accreditation of Laboratory Animal Care (AAALAC) International, and is Public Health Service-Assured (PHS assurance A3184-01). Briefly, airway (trachea and lung) tissues were collected from 24 mice (C57Bl/6j, 10-20 weeks), homogenized in 500 uL of phosphate-buffered saline (PBS), and used to inoculate five different solid growth media [tryptic soy (TS); TS + 5% sheep's blood; M9 minimal salts + 0.2% glucose; brain-heart infusion (BHI); and Luria broth (LB) (Teknova; Hollister, CA)] as well as three different BACTEC blood bottles [Plus Aerobic/F; Plus Anaerobic/F; and Lytic/10 Anaerobic/F (Becton Dickinson; Franklin Lakes, NJ)]. The inoculated solid growth media were incubated at 37C for seven days. The inoculated blood bottles were incubated with shaking (250 rpm) for 1-5 days, and 100 uL aliquots were periodically withdrawn for use in inoculating the five different solid growth media, which were then incubated at 37C for seven days. All colonies detected on the solid growth media were individually transferred to LB agar and, after further incubation at 37C for 1-3 days, streaked to single colonies on fresh LB agar. A representative single colony from each Petri plate was used to inoculate LB liquid and solid media, and these cultures incubated at 37C for 1-3 days for use in preparing frozen glycerol stocks as well as extraction of genomic DNA for sequencing. Sterile tissues (liver and spleen) that were collected from the same mice using a second set of dissection instruments were

processed in parallel, in order to recover contaminants of the bacterial isolation procedures [referred to as “background” (B) strains].

Genome Sequencing and Analysis

Extraction of high molecular weight DNA from overnight cultures of CPs was accomplished using the Nanobind CBB kit (PacBio catalog no.102-301-900). Barcoded sequencing libraries were prepared using the SMRTbell prep kit 3.0 (PacBio catalog no.102-141-700) with SMRTbell barcoded adapter 3.0 (PacBio catalog no.102-009-200) and using the Covaris g-TUBE shearing method to generate DNA fragments of 7-12 kb in length. Quantification of DNA concentrations was accomplished using the Qubit fluorometer method. The barcoded libraries were sequenced using a PacBio Sequel IIe system with HiFi workflows; one SMRT Cell 8M was used for run times of 15 hrs.

Raw sequencing reads were assembled using canu v2.2 with its standard options[67]. Resultant contigs were manually inspected, and BLAST was used to identify and remove duplicate assembled contigs. Phylogenetic placement in the GTDB release 202 system used the ANI-based script speciate.pl[68,69]. Phylogenomic analysis (Figure 1A) was performed using Species Tree Builder in KBase[70]. Genome assemblies were submitted to NCBI; assembly IDs are forthcoming.

Comparison of CP *versus* Airway Microbiome Phylogenetic Assignments

Sequencing reads from 4 independent 16S rRNA profiling investigations of the mouse airway microbiome[21–25] were aligned against refseq genome assemblies and placed into taxonomic groups using an established software pipeline called RapTOR. Sequence quality filtering was performed to remove low-quality ends as well as any partial primer sequences, as described previously[71,72]. The Duskmasker software tool was applied in order to remove low complexity and unidentified reads[73]. FASTQ sequences with low quality scores were then removed, followed by removal of any host sequences as identified through alignment against the mouse genome sequence (GRCm38) using Bowtie 2[74]. An additional precise alignment with mitochondrial and ribosomal genome sequences was performed to remove any of these host sequences. The remaining non-host (unaligned) sequences were then aligned to the Silva SSU database[75] using Bowtie 2 with local alignment settings. The generated “.sam” files were converted to “.taxsum” files using SAMtools[76] in a custom Perl script for each sample, producing a table for read abundance at each taxonomy level, with reads aligning equally well to multiple Silva entries placed through application of the lowest common ancestor (LCA) algorithm. Finally, reads mapping to each taxonomic group represented in a given profiling dataset were enumerated; and each group was assigned a rank based on the

relative abundance of reads mapping to it (i.e., the prominence with which it was represented in the profiling dataset). This information is summarized for the taxonomic groups to which the CPs [and, for comparison, the B strains (contaminants)] belong (Tables S1-3).

Lung Simulating Medium (LSM) Preparation

LSM was made according to Palmer (2006)[17]. Adjustments were made to the original formulation to increase sodium and chloride concentrations to more closely match those in healthy lungs. As a result, LSM contains 92mM NaCl, instead of 66.6mM NaCl as in SCFM[77]. Similarly, glucose concentration was increased to 5.5mM.

Competition Assays

3ml monocultures of individual CPs and *Bt* were inoculated from frozen glycerol stocks and grown in LSM at 37C with shaking (278rpm) for 24 hours. Cultures were then serially diluted again in LSM at a 1:50 ratio, and grown at 37C with shaking until late log phase, at which point the cultures were centrifuged at 3000g for 10 min and resuspended in fresh LSM. CPs were then diluted according to the ratios being tested, where a 1:1 ratio represented a cell suspension of 3.33×10^4 CFU/mL, a 0.1 ratio represented 3.33×10^3 CFU/mL, etc. After dilution, 3.33×10^4 CFU/ml of *Bt* was added to each 15ml CP dilution tube as well as to a *Bt*-only control. The 15ml volume was split into 5 3ml aliquots to make biological replicate assays. All samples were incubated at 37C with shaking for 24 h.

After 24 hours, samples were removed, diluted 1:100-1:100,000 in PBS, and plated onto LB plus carbenicillin (100µg/mL) to select for *Bt* colonies. Plates were incubated at 37C for 48 h or until colonies became visible, and colony forming units (CFU) were enumerated. Percent *Bt* growth was calculated by taking the CFU/ml of each replicate culture and dividing by the average of the CFU/ml in the *Bt*-only control and multiplying by 100. Dose-response curves and analyses were generated using the ECAnything algorithm in Graphpad Prism 10.

Phage Isolation and Plaque Assays

A 3ml culture of each CP was grown at 37C with shaking (278rpm) for 16 h, at which point 2ul of the culture were added to a well of a 2ml deep well plate containing 1ml of LB. These cultures were grown at 30C with shaking (750rpm) for 24 h, at which point each culture was back-diluted 1:70 and grown at 30C with shaking until it reached an OD of 1. To each of these 1ml cultures, 2ul of 3% hydrogen peroxide were added in

order to induce phage production. After incubation at 30C with shaking for 16 h, the cultures were centrifuged to pellet cells, and the supernatant was collected and sterilized using a 0.22uM filter. Ammonium sulfate was added to 30% saturation, and precipitate was collected by centrifugation at 16000g for 40 minutes at 4C. The supernatant was decanted, and the phage-containing precipitate was resuspended in 1ml of SM buffer (100mM NaCl, 8mM $MgSO_4$•$7H_2O$, 50mM Tris-Cl, 0.01% gelatin) and stored at 4ºC for use in plaque assays.

To perform plaque assays, 3ml of Bt was grown at 37C with shaking (278rpm) for 16 h, at which point it had reached stationary phase. Standard LB agar was prepared in 100x15mm Petri dishes (BD Biosciences) and allowed to cool. To create the soft agar overlay, 200ul of the Bt culture were mixed with 5ml molten LB soft agar (0.5%) and spread over the standard LB agar in each plate. The plates were allowed to cool for 20 min. Phage-containing precipitate was serially diluted 1:10, and 2ul of the solution was pipetted onto the soft agar and allowed to dry for 10 min. The plates were then incubated at 37C for 24 h, and the presence or absence of plaques was observed.

Supernatant Inhibition Experiments

CPs and *Bt* were grown in LSM monocultures as previously described. The cultures were diluted to $5x10^5$ CFU/ml, and each CP was combined with *Bt* in co-cultures; additionally, a *Bt*-only control was generated. The co-cultures were grown at 37C with shaking (278rpm) for ~72 h, centrifuged to pellet cells, and the supernatants collected and sterilized using a 0.22uM filter. The sterilized supernatant samples were pH adjusted to 7.03. Each supernatant sample was mixed 1:1 with 2X-concentrated LSM, and exponential-phase *Bt* was added to each mixture at $3.33x10^4$ CFU/mL. Growth curves were performed using a Tecan Spark plate reader, measuring OD600 every 0.25 h during growth at 37C with shaking (240rpm) for 30 h. Fold-change in maximum Bt CFU/ml reached was calculated by dividing the maximum CFU of Bt grown in supernatant from itself divided by the maximum CFU of Bt grown in supernatant from each CP co-culture.

Knockout of *sfp* in CP8

The CP8Δ*sfp* mutant was generated using a double-crossover homologous recombination method described previously[78]. Briefly, homologous arms were amplified up- and down-stream of the *sfp* gene using PCR, and the amplicon was cloned into the T2(2)-ori plasmid in addition to the oriT/traJ region which facilitates conjugative transfer using Golden Gate assembly. The resulting plasmid was introduced into CP8 using an established method for conjugation in *Bacillus*[79]. The transconjugants were plated onto

LB supplemented with kanamycin (20 µg/mL) and polymyxin B (5 µg/mL) to select for plasmid-bearing CP8. Colonies recovered from the selection plates were used to inoculate 3ml LB plus kanamycin (20 µg/mL), and the resulting cultures were grown at 37C with shaking (278rpm) for 16 h. 0.05 ml of each culture were then spread on an LB plus kanamycin (20 µg/mL) plate that was incubated at 45C for 16 h in order to induce the first crossover event. A single colony positive for the first crossover event by PCR was recovered from each plate and passaged 6 times in LB liquid culture. Liquid cultures were streaked onto 10 LB agar plates to generate single colonies. Replica plating of 96 colonies was performed to check for loss of kanamycin resistance, and PCR was used to screen for colonies in which *sfp* was absent. Resulting fragments and the 16S region were sequenced to confirm deletion and strain identity.

Growth Curves of CP8 and the CP8Δ*sfp* Mutant

CP8 and the CP8Δ*sfp* mutant were streaked on LB agar and incubated at 37C for 16 h. Single colonies were used to inoculate 3ml LB cultures in 14ml plastic tubes, and the cultures incubated at 37C with shaking (278rpm) until they reached early stationary phase. The cultures were then back-diluted to an OD of 0.1 in LB, and 100ul of the cell suspension were added to each well of a 96-well plate, generating 4 replicate assays per condition. Growth curves were performed using a Tecan Spark plate reader, measuring OD600 every 0.16 h during growth at 37C with shaking (240rpm) for 20 h.

Agar Diffusion Assays

Overnight cultures of *Bt* and CP8 were made in LSM as previously described. *Bt* was diluted to OD 0.5 and streaked onto LSM agar using a sterile cotton swab. Plates were briefly allowed to dry and 2ul spots of CP8 overnight culture were added. Plates were incubated at 37C and checked for the appearance of a zone of inhibition after 48 h.

Carbon Source Screening

Overnight cultures of CPs and *Bt* in LSM were generated as previously described. Cultures were centrifuged and the pelleted bacteria washed twice with 2x LSM with carbon sources removed. The bacteria were then diluted to an OD of 0.04, and 20 ul were added to each well of a 384-well plate in which individual carbon source from LSM were deposited to produce a final concentration of 10mM. Initial OD600 readings were taken using a plate reader, and then the plates were incubated at 30C with shaking (800rpm) for 3 days before a final OD600 reading was taken. Each CP or *Bt* was considered able to utilize a given carbon source if the final OD600 reading was greater than that of the blank plus 2 standard deviations.

Exometabolomics

Overnight cultures of CP7, CP8, CP19 and *Bt* were generated as previously described. The cultures were back-diluted 1:50 and then grown at 37C with shaking (278rpm) to late log phase. 3ml co-cultures were made in LSM combining *Bt* at $3.33x10^4$ CFU/ml with the relevant CP at its IC90. The co-cultures were incubated at 37C with shaking, and 1ml samples were collected at 24 h and 36 h. For collection, each sample was centrifuged at 3000rcf for 10 min, and the . supernatant was removed and syringe filtered to remove residual cellular material. Samples were analyzed via GC-TOF by the West Coast Metabolomics Center (Davis, CA). Data were SERRF normalized to remove batch effects, then normalized to the amount injected. Metabolite concentrations were normalized to a media-only control. For analysis, concentrations of each metabolite were converted to metabolite-contributed electrons using the oxidation-reduction half reaction for each metabolite analyzed. For carbon subset analysis, total electrons from lactate, proline, and aspartic acid in the co-culture supernatant at 24 hours were added. Electron concentrations below 0 indicate that a given metabolite is more abundant in co-culture than the media control.

Pairwise Combination Competition Assays

Pairwise combination competition assays were performed as described above ("Competition Assays") with the following adjustment. After resuspension in fresh media, the two CPs of interest were mixed together at a 1:1 ratio to generate the desired final CFU/ml (eg. for a 1:1 ratio with *Bt*, the two CPs were combined to generate a final concentration of $3.33x10^4$ CFU/ml). Subsequent dilutions were made and carried out as previously described.

Quantification of CP8, CP19 and Bt Growth in Co-Culture

qPCR primers and probes for the 16S rRNA region for CP8, CP19 and Bt were purchased from IDT with the following sequences:

Strain	Probe Sequence	Primer Sequences
CP8	/56-FAM/AAAGAGCGA/ZEN/CAGGGAAACAGTGCT/3IABkFQ/	CAGATCTGCCGGATTCATCTT
		CCGGCATTCTCCATCTCATT
CP19	/5SUN/CCAGATTCG/ZEN/CTTTCTCGACCGGATT/3IABkFQ/	GCAGACATGGGTGAAGAATTTG

		GGCGATTTCTACCGCTTCAT
Bt	/5Cy5/TGTCCGGAAAGAAATCATCCTGGCT/3IAbRQSp/	AGGCCTTCGGGTTGTAAAG
		GTAGTTAGCCGGTGCTTATTCT

To generate standard curves, overnight cultures of CP8, CP19 and Bt were made as previously described in LB. The following day, cultures were backdiluted 1:250 in LB and 1ml of each culture was collected at 11 timepoints. Optical density at each timepoint was measured (OD600 values ranged from 0.05 to 1.033) and cells were pelleted by centrifugation. Genome preparations were done on each pellet using the QIAgen DNeasy Powersoil kit (cat#47014). Concentrations of genomic DNA were quantified using the Qubit dsDNA Quantification Assay Kit (cat#Q32854). A 1:5 dilution of each sample was made to adjust DNA concentration to 3pg-100ng. PrimeTime Gene Expression Master Mix (cat#1055772) was used to run the qPCR reactions in triplicate, with 2ul of diluted genome preparation per well. Samples were analyzed using the BioRad CFX96 Touch Real-Time PCR detection system, with annealing at 60C. To create the standard curve, OD values were plotted against Cq values and a line was fit to the points.

To generate the growth curve, three biological replicates of CP8, CP19 and Bt were co-cultured in LSM at 37C and 278rpm for 36 hours, with 1ml collections made every hour between 4-30 hours post-inoculation and an additional collection made at 36 hours. Optical density measurements, DNA extraction and qPCR reaction preparation were performed as previously described. Samples were run in duplicate using the previously established conditions. Measured Cq values from the co-culture samples were converted to OD600 values for each organism using the previously generated standard curve.

Animal Models

These studies were carried out in strict accordance with the recommendations in the *Guide for the Care and Use of Laboratory Animals* and the National Institute of Health. All efforts were made to minimize suffering of animals. All animals were housed in ABSL2 conditions in an AAALAC-accredited and PHS-assured facility, and the protocol was approved by the Lawrence Livermore National Laboratory Institutional Animal Care and Use Committee (IACUC), which includes ethics in evaluation of protocols. Barrier-housed, specific pathogen-free 6 week old C57Bl/6j mice were acclimated prior to experiments. CP, *Bt*, and animal use were also approved by the Institutional Biosafety Committee (IBC).

Colonization Studies

Each CP was grown in monoculture in LB at 37C with shaking (250 rpm) for 16 h, recovered through centrifugation, resuspended in PBS, and diluted to an OD600 corresponding to 3.3×10^7 CFU/mL (based on prior determination of OD600-to-CFU plating efficiency measurements). 30 ul of this dosing material (corresponding to 10^6 CFU) were administered to the airway (via OPA) of each mouse. After 7 days, the trachea and lungs were collected and homogenized in PBS; dilutions (in PBS) were plated on LB agar; and, after 1-5 days at 37C, the CFU enumerated in order to assess CP load in the airway tissues.

Survival Studies

CP dosing material was generated and administered to mice as described above. After 3, 5 or 7 days, the mice were similarly administered (via OPA) 3×10^4 - 5×10^5 CFU of *Bt*. Weight, morbidity, and mortality were monitored for 10 days following *Bt* challenge; mice displaying ≥20% loss of body weight were euthanized.

Statistical analyses

Ordinary one-way ANOVA with Tukey's multiple comparisons test, ROC curve analyses, Mantel-Cox survival analyses, and all plotting of data to generate graphs, was completed using Graphpad Prism 10.

References

1. Costello, E. K. *et al.* Bacterial community variation in human body habitats across space and time. *Science* **326**, 1694–1697 (2009).
2. Santacroce, L. *et al.* The Human Respiratory System and its Microbiome at a Glimpse. *Biology* **9**, (2020).
3. Man, W. H., de Steenhuijsen Piters, W. A. A. & Bogaert, D. The microbiota of the respiratory tract: gatekeeper to respiratory health. *Nat. Rev. Microbiol.* **15**, 259–270 (2017).
4. Das, S. *et al.* A prevalent and culturable microbiota links ecological balance to clinical stability of the human lung after transplantation. *Nat. Commun.* **12**, 2126 (2021).
5. Bäumler, A. J. & Sperandio, V. Interactions between the microbiota and pathogenic bacteria in the gut. *Nature* **535**, 85–93 (2016).
6. Kamada, N., Chen, G. Y., Inohara, N. & Núñez, G. Control of pathogens and pathobionts by the gut microbiota. *Nat. Immunol.* **14**, 685–690 (2013).
7. Fangous, M. S. *et al.* Lactobacilli intra-tracheal administration protects from Pseudomonas aeruginosa pulmonary infection in mice - a proof of concept. *Benef. Microbes* **10**, 893–900 (2019).
8. Soner Yildiz, João P Pereira Bonifacio Lopes, Matthieu Bergé, Víctor González-Ruiz, Damian Baud, Joachim Kloehn, Inês Boal-Carvalho, Olivier P Schaeren, Michael Schotsaert, Lucy J Hathaway, Serge Rudaz, Patrick H Viollier, Siegfried Hapfelmeier, Patrice Francois, Mirco Schmolke. Respiratory tissue-associated commensal bacteria offer therapeutic potential against

pneumococcal colonization. *eLife* (2020).

9. Fauroux, B. *et al.* Burkholderia cepacia is associated with pulmonary hypertension and increased mortality among cystic fibrosis patients. *J. Clin. Microbiol.* **42**, 5537–5541 (2004).
10. Coenye, T., Vandamme, P., Govan, J. R. & LiPuma, J. J. Taxonomy and identification of the Burkholderia cepacia complex. *J. Clin. Microbiol.* **39**, 3427–3436 (2001).
11. Yu, Y. *et al.* Genomic patterns of pathogen evolution revealed by comparison of Burkholderia pseudomallei, the causative agent of melioidosis, to avirulent Burkholderia thailandensis. *BMC Microbiol.* **6**, 46 (2006).
12. Brett, P. J., DeShazer, D. & Woods, D. E. Burkholderia thailandensis sp. nov., a Burkholderia pseudomallei-like species. *Int. J. Syst. Bacteriol.* **48 Pt 1**, 317–320 (1998).
13. Kim, H. S. *et al.* Bacterial genome adaptation to niches: divergence of the potential virulence genes in three Burkholderia species of different survival strategies. *BMC Genomics* **6**, 174 (2005).
14. Günther, A. *et al.* Surfactant alterations in severe pneumonia, acute respiratory distress syndrome, and cardiogenic lung edema. *Am. J. Respir. Crit. Care Med.* **153**, 176–184 (1996).
15. Dickson, R. P., Erb-Downward, J. R. & Huffnagle, G. B. Towards an ecology of the lung: new conceptual models of pulmonary microbiology and pneumonia pathogenesis. *Lancet Respir Med* **2**, 238–246 (2014).
16. Dickson, R. P. & Huffnagle, G. B. The Lung Microbiome: New Principles for

Respiratory Bacteriology in Health and Disease. *PLoS Pathog.* **11**, e1004923 (2015).

17. Palmer, K. L., Aye, L. M. & Whiteley, M. Nutritional cues control Pseudomonas aeruginosa multicellular behavior in cystic fibrosis sputum. *J. Bacteriol.* **189**, 8079–8087 (2007).
18. Swart, A. L. *et al.* Pseudomonas aeruginosa breaches respiratory epithelia through goblet cell invasion in a microtissue model. *Nat. Microbiol.* **9**, 1725–1737 (2024).
19. Neve, R. L., Giedraitis, E., Akbari, M. S., Cohen, S. & Phelan, V. V. Secondary metabolite profiling of Pseudomonas aeruginosa isolates reveals rare genomic traits. *mSystems* **9**, e0033924 (2024).
20. Dunphy, L. J., Grimes, K. L., Wase, N., Kolling, G. L. & Papin, J. A. Untargeted metabolomics reveals species-specific metabolite production and shared nutrient consumption by Pseudomonas aeruginosa and Staphylococcus aureus. *mSystems* **6**, e0048021 (2021).
21. Barfod, K. K. *et al.* The murine lung microbiome in relation to the intestinal and vaginal bacterial communities. *BMC Microbiol.* **13**, 303 (2013).
22. Scheiermann, J. & Klinman, D. M. Three distinct pneumotypes characterize the microbiome of the lung in BALB/cJ mice. *PLoS One* **12**, e0180561 (2017).
23. Kostric, M. *et al.* Development of a stable lung microbiome in healthy neonatal mice. *Microb. Ecol.* **75**, 529–542 (2018).
24. Dickson, R. P. *et al.* The lung Microbiota of healthy mice are highly variable, cluster by environment, and reflect variation in baseline lung innate immunity. *Am. J. Respir. Crit. Care Med.* **198**, 497–508 (2018).

25. O'Dwyer, D. N. *et al.* Lung Microbiota contribute to pulmonary inflammation and disease progression in pulmonary fibrosis. *Am. J. Respir. Crit. Care Med.* **199**, 1127–1138 (2019).

26. Lloyd, D. P. & Allen, R. J. Competition for space during bacterial colonization of a surface. *J. R. Soc. Interface* **12**, 0608 (2015).

27. van Gestel, J., Weissing, F. J., Kuipers, O. P. & Kovács, A. T. Density of founder cells affects spatial pattern formation and cooperation in Bacillus subtilis biofilms. *ISME J.* **8**, 2069–2079 (2014).

28. Hsu, B. B. *et al.* Dynamic modulation of the gut Microbiota and metabolome by bacteriophages in a mouse model. *Cell Host Microbe* **25**, 803–814.e5 (2019).

29. Secor, P. R., Sass, G., Nazik, H. & Stevens, D. A. Effect of acute predation with bacteriophage on intermicrobial aggression by Pseudomonas aeruginosa. *PLoS One* **12**, e0179659 (2017).

30. Ulrich, R. L. *et al.* Characterization of the Burkholderia thailandensis SOS response by using whole-transcriptome shotgun sequencing. *Appl. Environ. Microbiol.* **79**, 5830–5843 (2013).

31. Ronning, C. M. *et al.* Genetic and phenotypic diversity in Burkholderia: contributions by prophage and phage-like elements. *BMC Microbiol.* **10**, 202 (2010).

32. Yu, Z.-C. *et al.* Filamentous phages prevalent in Pseudoalteromonas spp. confer properties advantageous to host survival in Arctic sea ice. *ISME J.* **9**, 871–881 (2015).

33. Carim, S. *et al.* Systematic discovery of pseudomonad genetic factors involved in

sensitivity to tailocins. *ISME J.* **15**, 2289–2305 (2021).

34. Blin, K. *et al.* antiSMASH 7.0: new and improved predictions for detection, regulation, chemical structures and visualisation. *Nucleic Acids Res.* **51**, W46–W50 (2023).
35. Aiosa, N. *et al.* Whole-Cell MALDI-ToF MS Coupled with Untargeted Metabolomics Facilitates Investigations of Microbial Chemical Interactions. *Chembiochem* **24**, e202200802 (2023).
36. Nakano, M. M., Corbell, N., Besson, J. & Zuber, P. Isolation and characterization of sfp: a gene that functions in the production of the lipopeptide biosurfactant, surfactin, in Bacillus subtilis. *Mol. Gen. Genet.* **232**, 313–321 (1992).
37. Quadri, L. E. *et al.* Characterization of Sfp, a Bacillus subtilis phosphopantetheinyl transferase for peptidyl carrier protein domains in peptide synthetases. *Biochemistry* **37**, 1585–1595 (1998).
38. Chen, X.-H., Koumoutsi, A., Scholz, R. & Borriss, R. More than anticipated - production of antibiotics and other secondary metabolites by Bacillus amyloliquefaciens FZB42. *J. Mol. Microbiol. Biotechnol.* **16**, 14–24 (2009).
39. Letarov, A. V. *et al.* Genetic analysis of the cold-sensitive growth phenotype of Burkholderia pseudomallei/thailandensis bacteriophage AMP1. *Sci. Rep.* **12**, 4288 (2022).
40. Ho, P.-Y., Nguyen, T. H., Sanchez, J. M., DeFelice, B. C. & Huang, K. C. Resource competition predicts assembly of gut bacterial communities in vitro. *Nat. Microbiol.* **9**, 1036–1048 (2024).
41. Levy, R. & Borenstein, E. Metabolic modeling of species interaction in the human

microbiome elucidates community-level assembly rules. *Proc. Natl. Acad. Sci. U. S. A.* **110**, 12804–12809 (2013).

42. Venturelli, O. S. *et al.* Deciphering microbial interactions in synthetic human gut microbiome communities. *Mol. Syst. Biol.* **14**, e8157 (2018).
43. Sonnenburg, E. D. *et al.* Specificity of polysaccharide use in intestinal bacteroides species determines diet-induced microbiota alterations. *Cell* **141**, 1241–1252 (2010).
44. Medlock, G. L. *et al.* Inferring metabolic mechanisms of interaction within a defined gut Microbiota. *Cell Syst.* **7**, 245–257.e7 (2018).
45. Redfield, A. C. On the proportions of organic derivatives in sea water and their relation to the composition of plankton. *James Johnstone Memorial Volume* 176–194.
46. Vecchio-Pagan, B., Bewick, S., Mainali, K., Karig, D. K. & Fagan, W. F. A Stoichioproteomic Analysis of Samples from the Human Microbiome Project. *Front. Microbiol.* **8**, 1119 (2017).
47. Rohmer, L., Hocquet, D. & Miller, S. I. Are pathogenic bacteria just looking for food? Metabolism and microbial pathogenesis. *Trends Microbiol.* **19**, 341–348 (2011).
48. Hurlbert, S. H. The measurement of niche overlap and some relatives. *Ecology* **59**, 67–77 (1978).
49. Petraitis, P. S. Likelihood measures of niche breadth and overlap. *Ecology* **60**, 703–710 (1979).
50. Smith, E. P. Niche breadth, resource availability, and inference. *Ecology* **63**, 1675 (1982).

51. Pierotti, M. E. R., Martín-Fernández, J. A. & Barceló-Vidal, C. The peril of proportions: robust niche indices for categorical data. *Methods Ecol. Evol.* **8**, 223–231 (2017).

52. Webb, N. E., Montefiori, D. C. & Lee, B. Dose-response curve slope helps predict therapeutic potency and breadth of HIV broadly neutralizing antibodies. *Nat. Commun.* **6**, 8443 (2015).

53. Regoes, R. R. *et al.* Pharmacodynamic functions: a multiparameter approach to the design of antibiotic treatment regimens. *Antimicrob. Agents Chemother.* **48**, 3670–3676 (2004).

54. Yagi, K., Huffnagle, G. B., Lukacs, N. W. & Asai, N. The Lung Microbiome during Health and Disease. *Int. J. Mol. Sci.* **22**, (2021).

55. de Melo Pereira, G. V., de Oliveira Coelho, B., Magalhães Júnior, A. I., Thomaz-Soccol, V. & Soccol, C. R. How to select a probiotic? A review and update of methods and criteria. *Biotechnol. Adv.* **36**, 2060–2076 (2018).

56. De Backer, D., Creteur, J., Zhang, H., Norrenberg, M. & Vincent, J. L. Lactate production by the lungs in acute lung injury. *Am. J. Respir. Crit. Care Med.* **156**, 1099–1104 (1997).

57. Bensel, T. *et al.* Lactate in cystic fibrosis sputum. *J. Cyst. Fibros.* **10**, 37–44 (2011).

58. Kottmann, R. M. *et al.* Lactic acid is elevated in idiopathic pulmonary fibrosis and induces myofibroblast differentiation via pH-dependent activation of transforming growth factor-β. *Am. J. Respir. Crit. Care Med.* **186**, 740–751 (2012).

59. Gillis, C. C. *et al.* Dysbiosis-associated change in host metabolism generates lactate to support Salmonella growth. *Cell Host Microbe* **23**, 54–64.e6 (2018).

60. Wu, X. *et al.* In vivo proteome of Pseudomonas aeruginosa in airways of cystic fibrosis patients. *J. Proteome Res.* **18**, 2601–2612 (2019).
61. Exley, R. M. *et al.* Neisseria meningitidis lactate permease is required for nasopharyngeal colonization. *Infect. Immun.* **73**, 5762–5766 (2005).
62. Gao, C. *et al.* Lactate utilization is regulated by the FadR-type regulator LldR in Pseudomonas aeruginosa. *J. Bacteriol.* **194**, 2687–2692 (2012).
63. Ayala, J. C. & Shafer, W. M. Transcriptional regulation of a gonococcal gene encoding a virulence factor (L-lactate permease). *PLoS Pathog.* **15**, e1008233 (2019).
64. Lozo Vukovac, E. *et al.* Bronchoalveolar pH and inflammatory biomarkers in patients with acute exacerbation of chronic obstructive pulmonary disease. *J. Int. Med. Res.* **47**, 791–802 (2019).
65. Su, S. *et al.* Construction and characterization of stable, constitutively expressed, chromosomal green and red fluorescent transcriptional fusions in the select agents, Bacillus anthracis, Yersinia pestis, Burkholderia mallei, and Burkholderia pseudomallei. *Microbiologyopen* **3**, 610–629 (2014).
66. Lagier, J.-C. *et al.* Microbial culturomics: paradigm shift in the human gut microbiome study. *Clin. Microbiol. Infect.* **18**, 1185–1193 (2012).
67. Koren, S. *et al.* Canu: scalable and accurate long-read assembly via adaptive k-mer weighting and repeat separation. *Genome Res.* **27**, 722–736 (2017).
68. Parks, D. H. *et al.* GTDB: an ongoing census of bacterial and archaeal diversity through a phylogenetically consistent, rank normalized and complete genome-based taxonomy. *Nucleic Acids Res.* **50**, D785–D794 (2022).

69. Mageeney, C. M., Trubl, G. & Williams, K. P. Improved Mobilome Delineation in Fragmented Genomes. *Front Bioinform* **2**, 866850 (2022).

70. Arkin, A. P. *et al.* KBase: The United States Department of Energy Systems Biology Knowledgebase. *Nat. Biotechnol.* **36**, 566–569 (2018).

71. Vandernoot, V. A. *et al.* cDNA normalization by hydroxyapatite chromatography to enrich transcriptome diversity in RNA-seq applications. *Biotechniques* **53**, 373–380 (2012).

72. Bent, Z. W. *et al.* Transcriptomic analysis of Yersinia enterocolitica biovar 1B infecting Murine macrophages reveals new mechanisms of extracellular and intracellular survival. *Infect. Immun.* **83**, 2672–2685 (2015).

73. Morgulis, A., Gertz, E. M., Schäffer, A. A. & Agarwala, R. A fast and symmetric DUST implementation to mask low-complexity DNA sequences. *J. Comput. Biol.* **13**, 1028–1040 (2006).

74. Langmead, B. & Salzberg, S. L. Fast gapped-read alignment with Bowtie 2. *Nat. Methods* **9**, 357–359 (2012).

75. Quast, C. *et al.* The SILVA ribosomal RNA gene database project: improved data processing and web-based tools. *Nucleic Acids Res.* **41**, D590–6 (2013).

76. Danecek, P. *et al.* Twelve years of SAMtools and BCFtools. *Gigascience* **10**, (2021).

77. Jayaraman, S., Joo, N. S., Reitz, B., Wine, J. J. & Verkman, A. S. Submucosal gland secretions in airways from cystic fibrosis patients have normal [Na^+] and pH but elevated viscosity. *Proceedings of the National Academy of Sciences* **98**, 8119–8123 (2001).

78. Qi, G. *et al.* Deletion of meso-2,3-butanediol dehydrogenase gene budC for enhanced D-2,3-butanediol production in Bacillus licheniformis. *Biotechnol. Biofuels* **7**, 16 (2014).

79. Heinze, S. *et al.* Transmating: conjugative transfer of a new broad host range expression vector to various Bacillus species using a single protocol. *BMC Microbiol.* **18**, 56 (2018).

CP	Species	Relative IC50	95% CI	*Bt* growth at a 1:1 ratio (%)	Niche Index
CP7	*Pseudomonas stutzeri*	0.001172	0.0006442-0.003346	1.893	0.875
CP4	*Pseudomonas fluorescens*	0.003086	0.001791-0.005331	3.200	0.869
CP19	*Brevibacillus borstelensis*	0.006604	0.006484 - 0.01141	3.046	0.775
CP17	*Bacillus megaterium*	5738	3598 – n.d.	98.99	0.704
CP18	*Peribacillus frigoritolerans*	0.0001693	0.0001633 - 0.0001850	0.534	0.591
CP20	*Bacillus clausii*	n.d.	n.d.	115.2	0.457
CP26	*Bacillus licheniformis*	n.d.	n.d.	260.0	0.433
CP13	*Bacillus licheniformis*	n.d.	n.d.	913.0	0.421
CP9	*Neisseria lactamica*	n.d.	n.d.	157.1	0.357
CP8	*Bacillus velezensis*	2.316	0.8280 – 5.073	56.97	0.351

Table 1 Summary of pathogen inhibition by CPs. Relative IC50 values and 95% confidence intervals (95% CI) are shown for each inhibitory CP. Not determined (n.d.) indicates that a value could not be measured. CPs are listed in order of decreasing NI values.

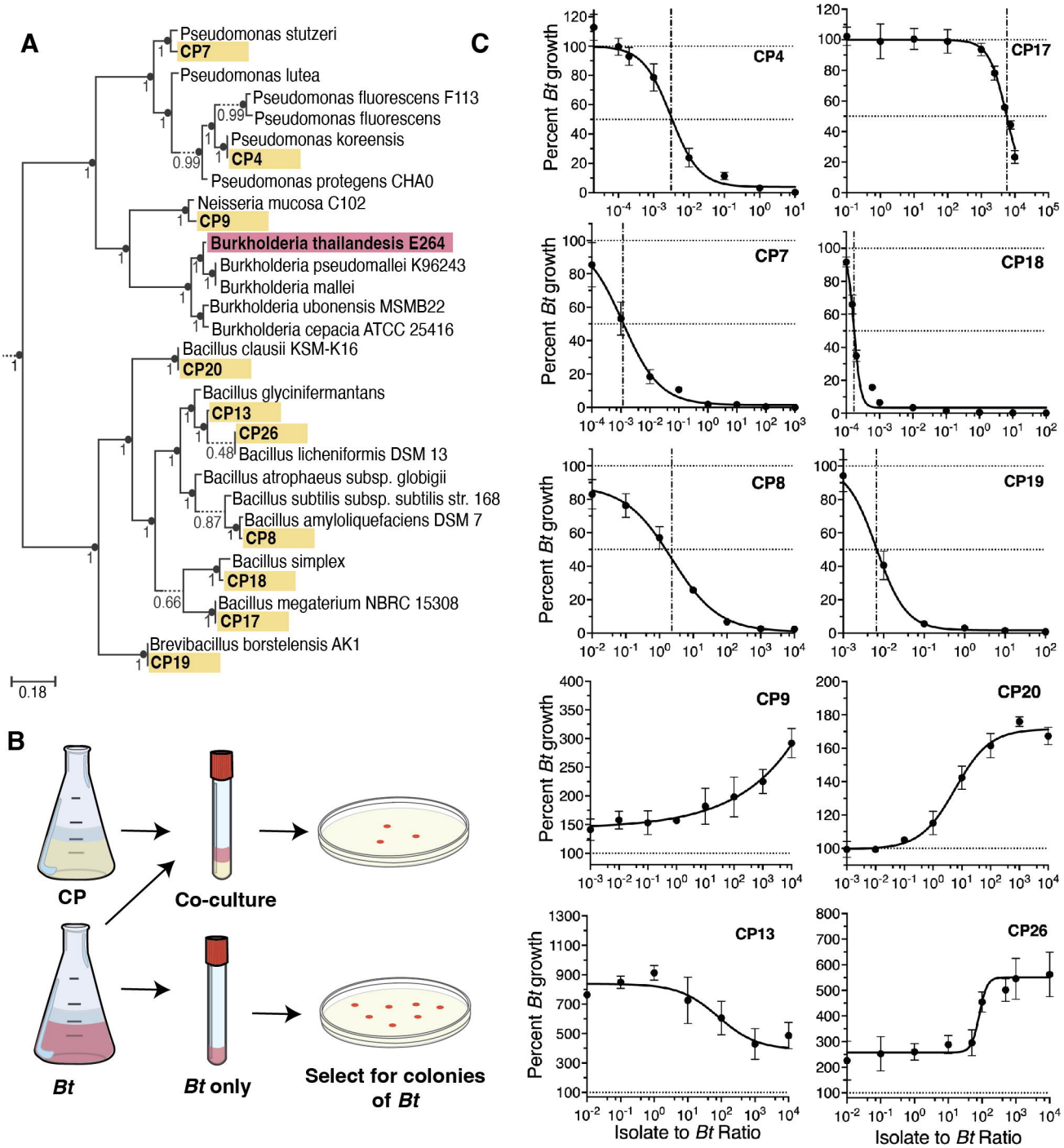

Figure 1 Characterization of CP activity against *B. thailandensis* in vitro. (A) Phylogenomic tree of CPs (yellow) and model pathogen *B. thailandensis* (Bt) (red), interspersed amongst publicly available genomes (no color). (B) Schematic of competition assay used to test in vitro inhibitory capabilities. Percent growth of *Bt* is calculated as the CFU in co-culture at 24 hours divided by the CFU in the *Bt* monoculture at 24 hours multiplied by 100. Co-culture inhibition was tested for multiple starting densities of CP (see Figure 1C x-axis). Starting density of *Bt* and CP at a 1:1 ratio are 3.33x104 CFU/ml per organism. *Bt* monoculture is inoculated at 3.33×10^4 CFU/ml. (C) Dose-response curves for CPs against Bt. Relative IC50 is denoted with a vertical dashed-dotted line, and 100% and 50% growth are denoted with horizontal dotted lines. Percent growth at each density is represented as mean ± SEM.

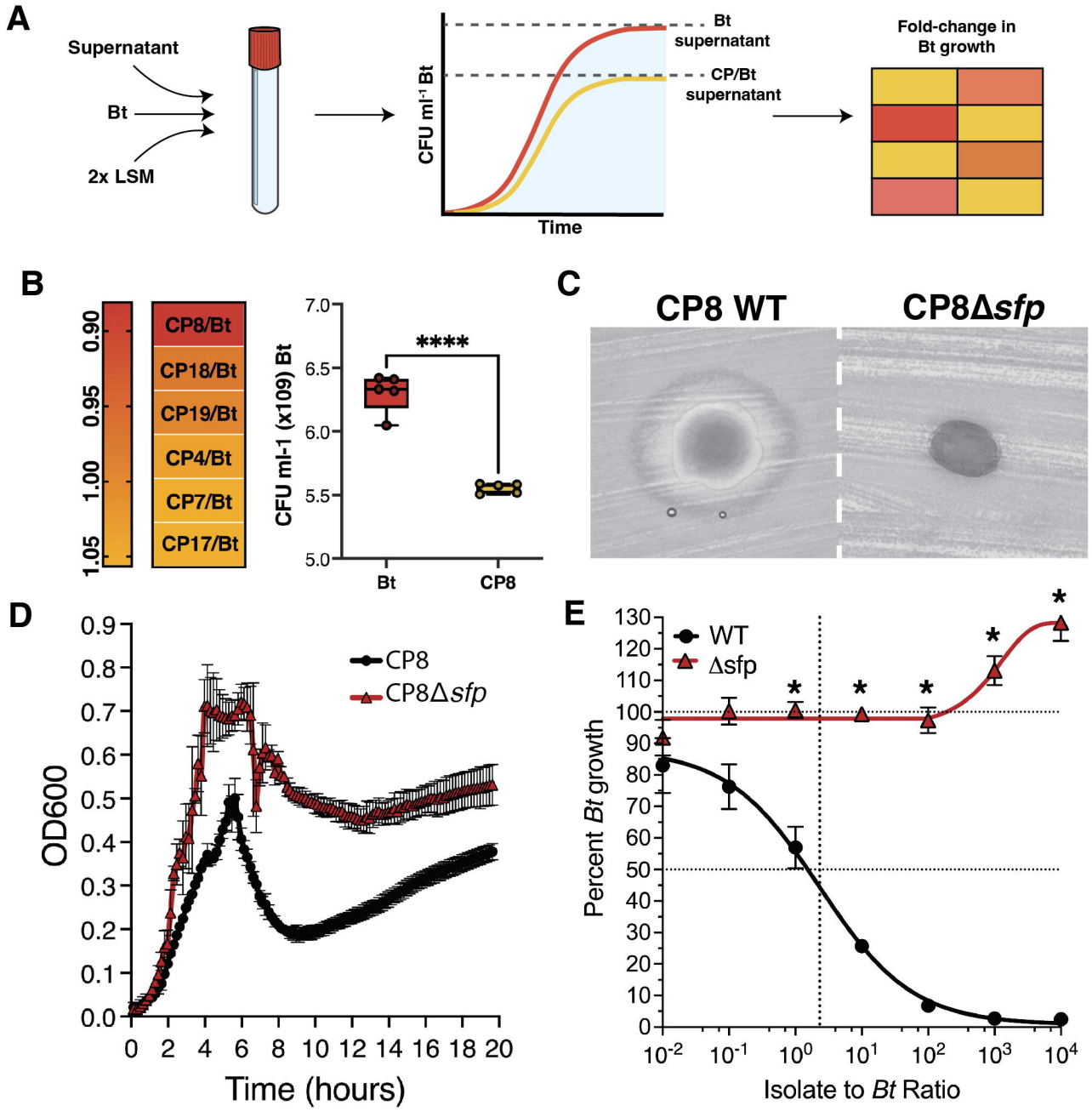

Figure 2 Production of a specialized metabolite plays a role in the antagonistic activities of CP8. (A) Schematic representation of supernatant inhibition experiment workflow. Supernatant from a *Bt* and CP co-culture or from *Bt* monoculture (supernatant) is mixed 1:1 with 2x LSM. This mixture is used as the growth medium for subsequent *Bt* growth curves. Fold-change in *Bt* growth is calculated by dividing the maximum growth of *Bt* in co-culture supernatant by the maximum growth of *Bt* grown in supernatant from itself. (B) Left: Heatmap of fold-change in max CFU of *Bt* grown in supernatant from each inhibitory CP and *Bt* co-culture relative to *Bt* grown in supernatant from itself. Co-culture supernatant was collected at 72 hours. A fold-change of 1 indicates no difference in growth in co-culture supernatant compared to *Bt* growth in supernatant from itself. A fold-change less than 1 indicates a reduction in pathogen growth. Right: Boxplot of growth inhibition by CP8 supernatant. Data are represented as mean ± SD. (C) Agar diffusion assays testing the CP8 wildtype strain (CP8 WT) and sfp mutant strain (CP8Δsfp) for inhibition of Bt after 48 hours. (D) Growth curves of CP8 WT (black) and CP8Δsfp (red) (E) Dose-response curve of CP8 WT (black) and CP8Δsfp (red) against Bt after 24 hours of co-culture. Percent growth at each density is represented as mean ± SEM.

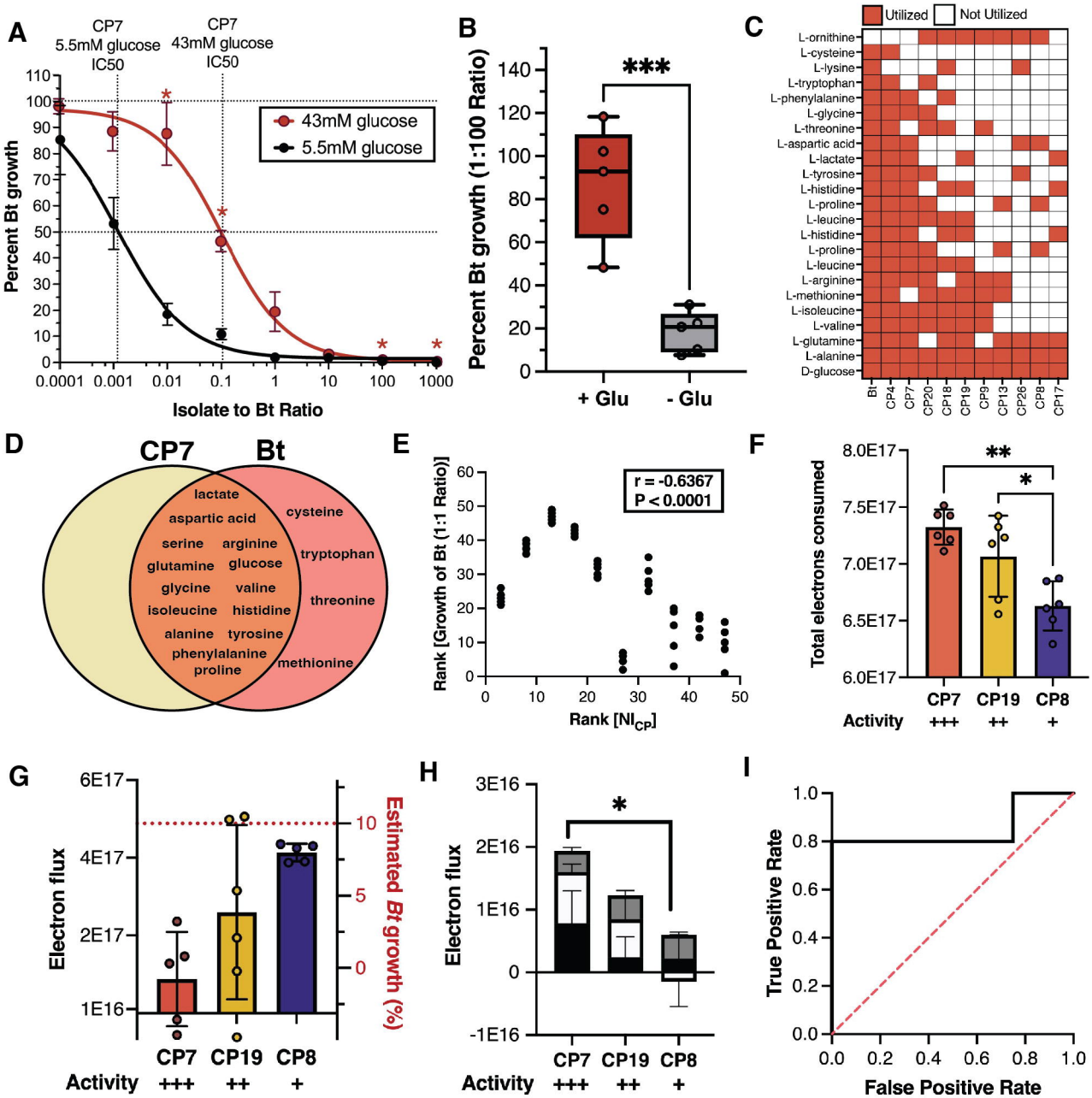

Figure 3 Metabolic niche overlap is indicative of pathogen and CP antagonism. (A) Dose-response curve for CP7 grown in unsupplemented LSM (black) or with additional glucose (red). Percent growth at each density is represented as mean ± SEM. (B) Activity of CP7 against Bt at a 1:100 ratio with or without glucose supplementation (red and gray, respectively). Data are summarized as mean ± SD. ***P<0.001. (C) Carbon utilization heatmap for CPs and Bt. (D) Venn diagram of carbon sources utilized by CP7 and Bt. (E) Plot of rank percent *Bt* growth at a 1:1 ratio after 24 hours vs rank of Niche Index for each CP. Correlation is determined by Spearman rank correlation (r = -0.6367, P < 0.0001, 95% CI [-0.7891 -0.4261], N = 49). (F) Total carbon consumed by CPs grown in combination with Bt at 36 hours (mean ± SD). Activity indicates relative amount of Bt inhibition at a 1:1 ratio from most (+++) to least (+) inhibitory. *P=0.05; **P<0.01. (G) Total electron flux at 24 hours. Red dashed line indicates the estimated abundance of *Bt* in each co-culture. (H) Summed electron flux of lactate (black), proline (white), and aspartic acid (gray) at 24 hours in different CP co-culture conditions (mean ± SD). *P<0.05.(I) Receiver operator characteristic curve showing the ability of growth on lactate to distinguish inhibitory CPs from non-inhibitory CPs. An AUROC of 1 indicates perfect distinction between inhibitors and non-inhibitors; an AUROC of 0.5 (dashed red line) indicates no distinction between inhibitors and non-inhibitors.

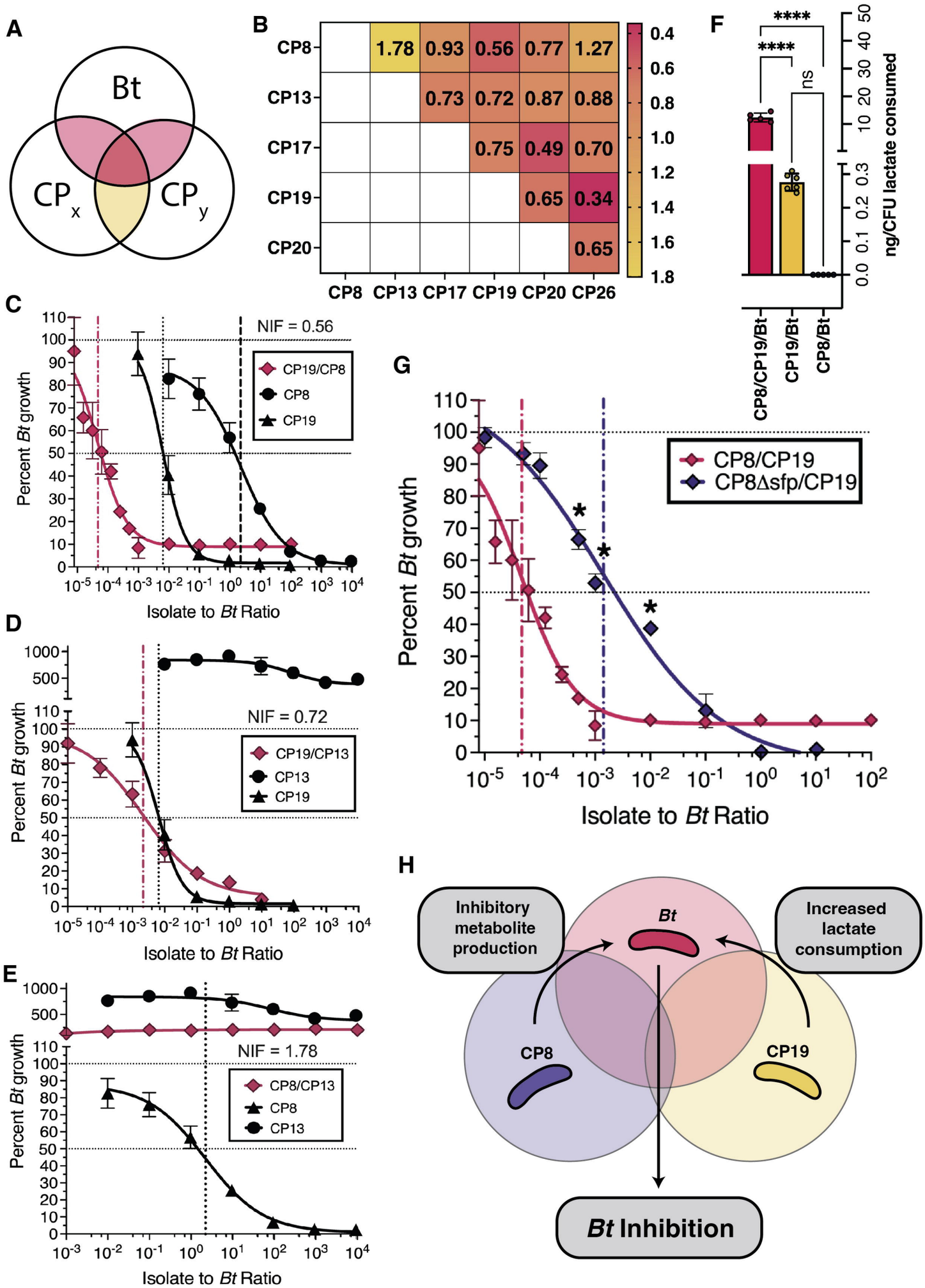

Figure 4 Niche overlap aids in identification of efficacious CP combinations. (A) Venn diagram representation of the Niche Index Fraction (NIF) calculation. Yellow represents the fraction numerator and red the denominator. (B) Heatmap of NIF values for each colonizing CP. (C) Dose-response curve for the CP8/CP19 combination (mean ± SEM). (D) Dose-response curve for the CP19/CP13 combination (mean ± SEM). (E) Dose-response curve for the CP13/CP8 combination (mean ± SEM). (F) Lactate consumed (as determined via GC-TOF) for 3 conditions, normalized to CFU of each CP inoculated (mean ± SD). ****P<0.0001. (G) Dose-response curve for the CP8/CP19 (red) and CP8sfp/CP19Δsfp (black) combinations. (H) Schematic of the proposed mechanism for *Bt* inhibition by the CP8/CP19 combination. CP8 produces a specialized metabolite that inhibits growth of the *Bt*. Additionally, increased lactate consumption by CP19 in the presence of CP8 further reduces *Bt* growth. Overall, minimal niche overlap between the CPs, and high overlap with *Bt*, allows for further inhibition of *Bt* with minimal inter-CP antagonism.

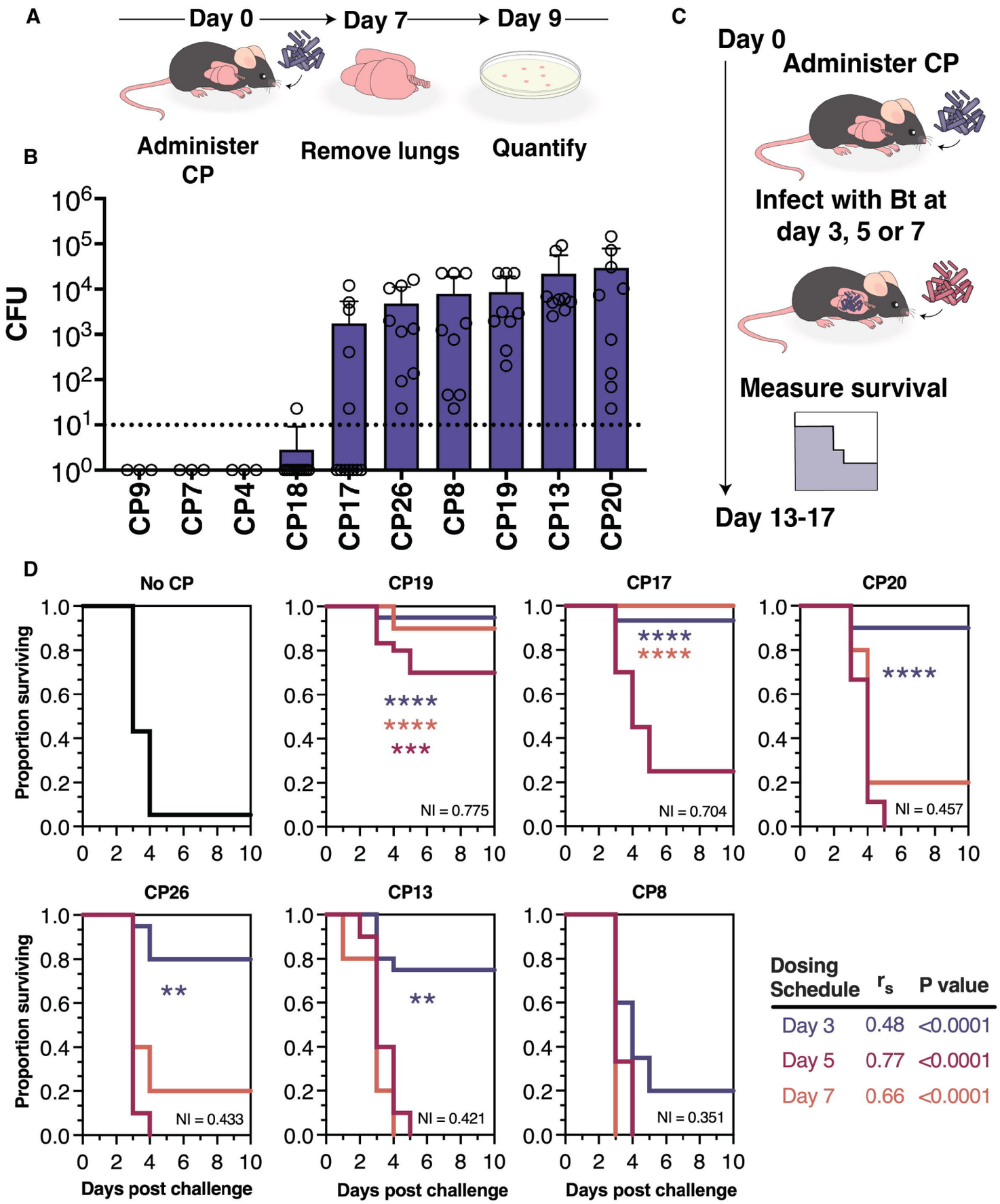

Figure 5 CPs colonize the mouse airway, and protect against respiratory *Bt* infection. (A) Schematic of colonization testing for CPs. Each CP (10^6 CFU) is administered to the lower airway via OPA.. After 7 days, the airway tissues (lungs and trachea) are collected, homogenized, and plated in order to enumerate viable CPs (expressed as CFU per tissue homogenate). (B) Colonization results from airway tissues collected at 7 days following CP administration. The dotted line represents the minimum CFU at which the CP is considered able to colonize in a reliably detectable manner. Data are represented as the mean ± SD. (C) Schematic of the method for survival testing. Each CP (10^6 CFU) is administered to the lower airway via OPA; and then, at 3, 5, or 7 days post-CP, challenged with a normally lethal dose of *Bt* ($3x10^4$ - $5x10^5$ CFU). Survival is measured over the course of 10 days post-*Bt*. (D) Survival data from mice administered no CP (vehicle control), CPs at 3 days (blue), 5 days (orange), or 7 days (red) prior to *Bt* challenge. The Niche Index value for each CP is listed in the lower-right corner of its associated graph. Comparison of survival rate with versus without CP treatment was accomplished using the Mantel-Cox test ****P<0.0001, ***P<0.0002, **P<0.01. A summary of the relationship between days surviving and Niche Index value for each dosing schedule is also shown.

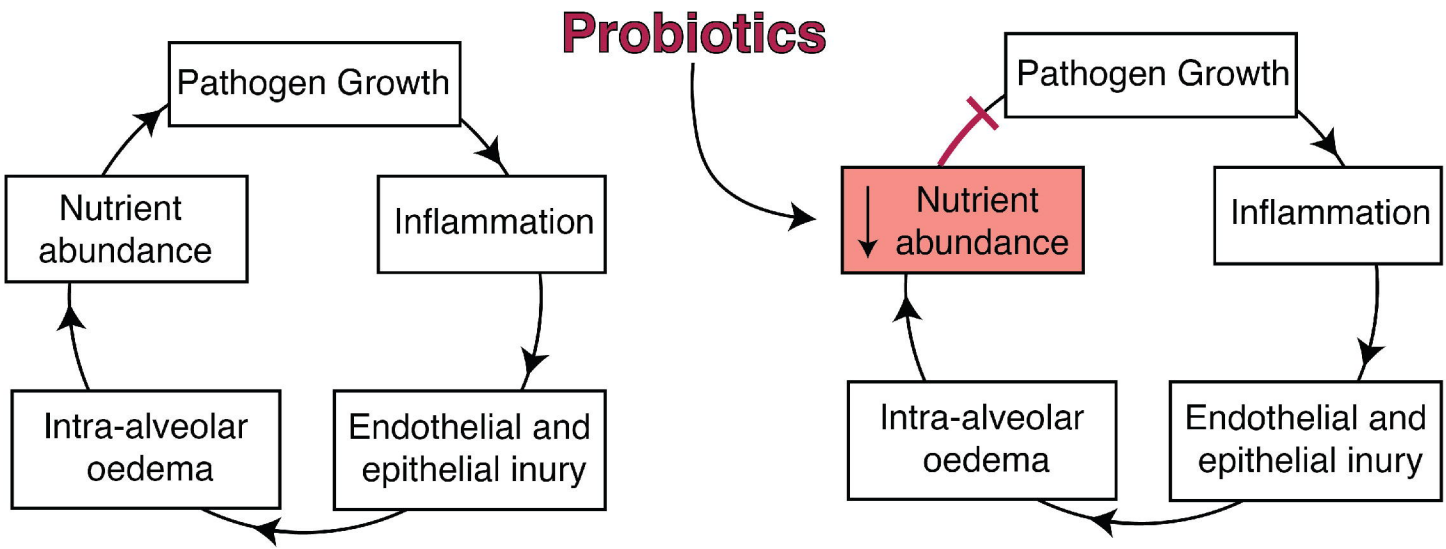

Figure 6 Proposed mechanism of CP protection. Left: During lower airway infection, bacterial growth elicits inflammation from the host, with concurrent endothelial and epithelial injury. Intra-alveolar oedema introduces additional nutrients from the blood into the alveoli and lung lumen, enabling further growth of the pathogen. This positive feedback loop results in uncontrolled growth of the pathogen, ultimately facilitating its instantiation. Right: Probiotics delivered directly to the lower airway may limit infection by reducing nutrient abundance after oedema, which prevents further growth of the pathogen and thereby breaks the infection-promoting feedback loop.